RESEARCH ARTICLE

Key Points:
- Secondary flow in symmetrical bifurcations causes strong near-bed flow curvature
- A disproportional amount of near-bed flow enters the dominant downstream channel
- Flow curvature adds a stabilizing feedback on bifurcation evolution

Correspondence to:
W. A. Marra,
w.a.marra@uu.nl

Near-bed and surface flow division patterns in experimental river bifurcations

Wouter A. Marra[1,2], Daniel R. Parsons[2,3], Maarten G. Kleinhans[1], Gareth M. Keevil[2], and Robert E. Thomas[2,3]

[1]Faculty of Geosciences, Universiteit Utrecht, Utrecht, Netherlands, [2]School of Earth and Environment, University of Leeds, Leeds, UK, [3]Now at: Department of Geography Environment and Earth Sciences, University of Hull, Hull, UK

Abstract Understanding channel bifurcation mechanics is of great importance for predicting and managing multichannel river processes and avulsion in distributary river deltas. To date, research on river channel bifurcations has focused on factors determining the stability and evolution of bifurcations. It has recently been shown that, theoretically, the nonlinearity of the relation between sediment transport and flow discharge causes one of the two distributaries of a (slightly) asymmetrical bifurcation to grow and the other to shrink. The positive feedback introduced by this effect results in highly asymmetrical bifurcations. However, there is a lack of detailed insight into flow dynamics within river bifurcations, the consequent effect on bed load flux through bifurcating channels, and thus the impact on bifurcation stability over time. In this paper, three key parameters (discharge ratio, width-to-depth ratio, and bed roughness) were varied in order to examine the secondary flow field and its effect on flow partitioning, particularly near-bed and surface flow, at an experimental bifurcation. Discharge ratio was controlled by varying downstream water levels. Flow fields were quantified using both particle image velocimetry and ultrasonic Doppler velocity profiling. Results show that a bifurcation induces secondary flow cells upstream of the bifurcation. In the case of unequal discharge ratio, a strong increase in the secondary flow near the bed causes a larger volume of near-bed flow to enter the dominant channel compared to surface and depth-averaged flow. However, this effect diminishes with larger width-to-depth ratio and with increased bed roughness. The flow structure and division pattern will likely have a stabilizing effect on river channel bifurcations. The magnitude of this effect in relation to previously identified destabilizing effects is addressed by proposing an adjustment to a widely used empirical bed load nodal-point partition equation. Our finding implies that river bifurcations can be stable under a wider range of conditions than previously thought.

1. Introduction

River deltas contain key nodes where fluid and sediment are partitioned into smaller channels. The mechanisms governing the division of flow and sediment at these channel bifurcations essentially control downstream water and sediment partitioning and, in many cases, also result in an upstream backwater control [see *Slingerland and Smith*, 2004; *Kleinhans et al.*, 2013, for review]. The control of flow and sediment partitioning means that bifurcation evolution and stability is intrinsically linked with these mechanics [*Kleinhans et al.*, 2008] and, thus, plays a significant role in the evolution of deltaic systems [*Wang et al.*, 1995; *Kleinhans et al.*, 2008; *Edmonds and Slingerland*, 2008]. Bifurcations are also a key control of braided river system behavior [*Repetto et al.*, 2002; *Bolla Pittaluga et al.*, 2003; *Federici and Paola*, 2003; *Bertoldi and Tubino*, 2005, 2007; *Miori et al.*, 2006; *Parsons et al.*, 2007]. Understanding river channel bifurcation behavior is hence of great importance for managing fluvio-deltaic and braided river plains, notably in prediction and management of flood risks and understanding the evolution of braided river systems and river delta environments in the face of environmental change.

The inherent instability of bifurcations has traditionally been explored and explained using numerical models and linear stability analysis [see review in *Kleinhans et al.*, 2013]. A qualitative description of the stability analysis is as follows. Given a nearly symmetrical bifurcation with one slightly deeper and one slightly shallower bifurcate, the slightly deeper bifurcate has a slightly higher discharge and flow velocity. As sediment transport is known to depend nonlinearly on flow velocity, the sediment transport capacity in the deeper bifurcate is somewhat larger than in the shallower branch. However, in the absence of topographic or

curvature-induced steering, the sediment transported through the upstream channel is partitioned between the downstream channels in proportion to the bifurcate widths [*Bolla Pittaluga et al.*, 2003]. Consequently, the sediment supplied to the slightly deeper bifurcate is smaller than the transport capacity, and this dominant channel incises. Channel deepening leads to a positive feedback wherein more water is drawn into the dominant bifurcate and more incision occurs, while the subordinate channel has reduced discharge and sediment transport capacity. As a result, the bifurcation is unstable and will become increasingly asymmetric [*Wang et al.*, 1995; *Bolla Pittaluga et al.*, 2003]. A key point of such linear stability analyses is that they evaluate the initial stability without taking the consequent morphological development into account. In the example above, the channel widths are constant and equal for both bifurcate channels. In erodible channels, the morphology will adapt to such cases over time. The study in this paper focuses on how the morphology might adapt.

Further research has focused on the effect of bifurcation angle [*Klaassen and Masselink*, 1992], the influence of downstream water surface slope boundary conditions [*Wang et al.*, 1995; *Kleinhans et al.*, 2013; *Thomas et al.*, 2011], the morphological characteristics of bifurcations initiated by bar formation [*Bertoldi and Tubino*, 2005, 2007; *Federici and Paola*, 2003; *Repetto et al.*, 2002], the stability and evolution of bifurcations with erodible banks [*Miori et al.*, 2006; *Edmonds and Slingerland*, 2009; *Kleinhans et al.*, 2008, 2011], and the effect of bends upstream of bifurcations [*Kleinhans et al.*, 2008]. A curved channel upstream of the bifurcation causes helical flow, which strongly affects the sediment transport direction [*Kleinhans et al.*, 2008] and thus controls sediment partitioning. All these effects point to the importance of secondary flow structures, which modify the sediment partitioning between the two bifurcates. This suggests that a perturbation of the detailed flow structure at a perfectly symmetrical bifurcation may also trigger the destabilization of the bifurcation. Moreover, if a perfectly symmetrical bifurcation is not perturbed at the bed but within the inherited flow field, the detailed flow structure determines the partitioning of bed load transport and the initial aggradation or erosion of the downstream channels.

Previous work by *Thomas et al.* [2011] showed that secondary flow cells develop in the bifurcate channels which flow toward the inner bank at the surface. Their work mainly investigated the effect of the internal bifurcation angle on the partitioning of the flow, which had little to no influence, and the flow structure in the bifurcate channels that resulted from a range of discharge divisions ratios. An interesting observation from those experiments is that near-bed flow seemed to be steered stronger into the bifurcate channel with the highest discharge.

The objective of this paper is to investigate the detailed flow structure in a perfectly symmetrical bifurcation flume that is perturbed by a slight difference in discharge conveyance in the two bifurcate channels. We focus particularly on the near-bed flow direction as this drives the sediment transport at the onset of bifurcation destabilization. In our experiments, the discharge partitioning was unbalanced by adjusting the downstream weirs in both bifurcate channels, which has the consequence that flow at the bifurcation is preferentially curved toward the channel with the highest discharge. Helical flow intensity is inversely proportional to the bend radius relative to the channel width and depth, and inversely proportional to the Nikuradse roughness length (bed roughness) relative to channel depth. Therefore, we further vary bed roughness and width-to-depth ratio. To isolate the effect of the bifurcating planform from changes in depth or gradient advantages, we also performed control experiments where the water depths were kept equal in the upstream channel and both downstream channels. In addition to similar flow measurements [*Thomas et al.*, 2011], we utilize Particle Image Velocimetry to elucidate the flow structure very near the bed. Building on these data, we study overall flow structure and near-bed flow steering for a wide range of variables known to be relevant to bifurcation stability, namely discharge division, width-to-depth ratio and bed roughness.

2. Methods and Materials

2.1. Experimental Setup

We conducted a series of experiments to systematically investigate the flow structure in relation to three key variables. First, we varied the width-to-depth ratio (WDR) of the incoming channel by lowering flow discharge and reducing downstream weir height to maintain uniform flow conditions at the system scale. As wider, shallower, channels tend to have lower secondary flow intensities, the experiment was targeted at examining the importance of WDR on flow partitioning at bifurcations. Second, within the WDR experiments
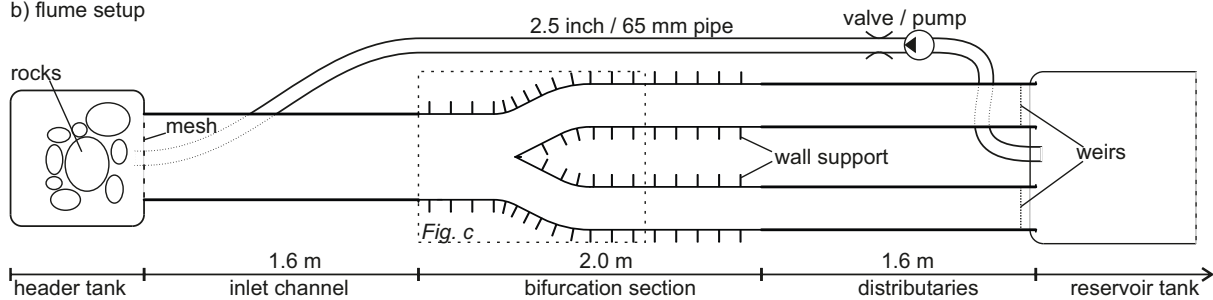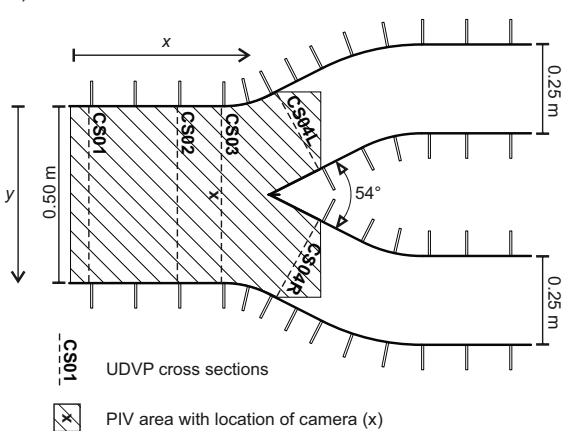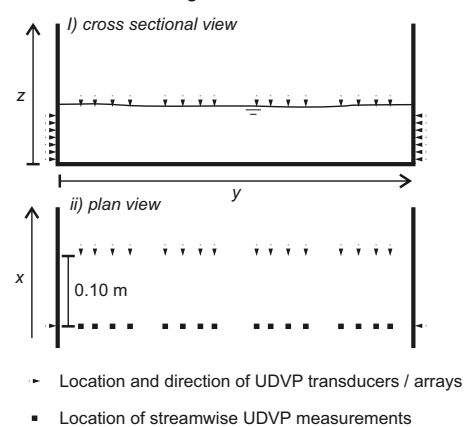
Figure 1. (a) Photograph of the model setup, (b) schematic illustration of the model setup, (c) bifurcation model detail with locations of UDVP measurement cross sections and PIV area. (d) Illustration of the locations and directions of UDVP transducers in the upstream part of the bifurcation at low WDR. In the bifurcate channels, eight measurements per channel width were used. In the high-WDR runs, three vertical measurement locations were used.

we also varied downstream water levels in the bifurcate channels in order to introduce a gradient advantage for one channel. This led to asymmetric discharge partitioning and strengthened secondary flows, allowing us to examine the interaction of secondary flow with WDR under asymmetric conditions. Third, we varied bed roughness by running experiments initially with a smooth bed and subsequently with an immobile gravel bed. This set of experiments was designed to capture the dampening influence of increased roughness on secondary flows and how this interacts with WDR in governing the mechanics of partitioning.

The experiments were conducted in a transparent Perspex bifurcation scale model (Figures 1a and 1b), with a 1.6 m long, 0.5 m wide inlet channel upstream of a bifurcation which splits the flow into two 0.25 m wide, 1.6 m long, distributaries (the same model as the 54° setup used by *Thomas et al.* [2011]). The entire setup was tilted at a slope of 1×10^{-3}. Water was pumped from a reservoir into a header tank. This header tank was filled at a controlled rate from below and contained a layer of rocks at the bottom to break any

Table 1. Experiment Design Parameters and Flow Properties[a]

Property	Location	Run							
		80EQ	80NEQ	35EQ	35NEQ	80EQ S	80NEQ_S	35EQ_S	35NEQ_S
WDR		Low (6.3)	Low (6.3)	High (14.3)	High (14.3)	Low (6.3)	Low (6.3)	High (14.3)	High (14.3)
Symmetry (Qr)		Symmetry (1)	Asymmetry (1.5)	Symmetry (1)	Asymmetry (1.5)	Symmetry (1)	Asymmetry (1.5)	Symmetry (1)	Asymmetry (1.5)
Bed		Smooth	Smooth	Smooth	Smooth	Rough	Rough	Rough	Rough
H (m)	CS01-04	0.080	0.080	0.035	0.035	0.080	0.080	0.035	0.035
Ux_{av} (m/s)	CS01-03	0.18	0.18	0.16	0.15	0.14	0.15	0.09	0.06
	CS04L	0.18	0.14	0.16	0.10	0.14	0.12	0.07	0.04
	CS04R	0.18	0.23	0.16	0.18	0.15	0.17	0.06	0.06
Fr	CS01-03	0.20	0.20	0.28	0.26	0.16	0.17	0.15	0.10
Re	CS01-03	10298	10358	4720	4396	8320	8605	2524	1765
We	CS01-03	426.6	431.5	152.8	132.5	278.5	297.9	43.9	21.6
Q (m^3/s $\times10^{-3}$)	CS01	7.28	7.22	2.85	2.69	5.71	6.02	1.65	1.16
	CS02	7.14	7.16	2.83	2.62	5.74	6.00	1.41	1.10
	CS03	7.03	7.21	2.81	2.60	5.90	5.91	1.49	0.92
	CS04L+R	7.08	7.25	2.78	2.49	5.80	5.87	1.17	0.91
	CS04L	3.56	2.71	1.37	0.88	2.85	2.40	0.61	0.36
	CS04R	3.52	4.54	1.41	1.61	2.95	3.47	0.55	0.55
Q_{rms} (m^3/s $\times10^{-3}$)	CS01-04	0.09	0.03	0.03	0.07	0.07	0.06	0.17	0.11
Q_{rms} (%)	CS01-04	1.33	0.46	0.89	2.72	1.24	1.08	12.16	10.73
$Qr(Q_{right}/Q_{left})$	CS04	0.99	1.67	1.03	1.83	1.03	1.45	0.90	1.51
Q_{right}/Q_{total}	CS04R	0.50	0.63	0.51	0.65	0.51	0.59	0.47	0.60
$q_{surf,right}/q_{surf,total}$	PIV surface	0.51	0.62	0.50	0.56	0.49	0.55	0.50	0.51
$q_{bed,right}/q_{bed,total}$	PIV bed	0.52	0.71	0.50	0.68				
$|\hat{\Gamma}|$	CS01	15.4	12.8	5.5	0.9	8.5	9.0	2.1	4.0
	CS02	14.6	10.8	1.2	1.0	6.0	8.1	1.3	4.3
	CS03	12.7	10.3	0.9	1.5	6.8	10.0	2.9	4.5
	CS04L	18.0	29.9	9.9	7.1	24.4	31.5	8.4	8.5
	CS04R	13.1	16.3	8.2	4.0	27.6	23.9	5.4	10.2

[a]WDR, Symmetry and Bed are the varied properties and desired values for the different runs. Remaining data are measurements from UDVP and PIV data. Flow division ratios from PIV data were derived from the data in Figure 7 and represent the location of the division line in this figure at $y/W = 1$.

inherited flow structure. From the header tank, the water flowed downstream through a series of flow straightening baffles into the upstream channel of the flume. The inlet flow was tested and adjusted to ensure the best possible upstream boundary conditions as will be demonstrated with measurements.

The water level and water surface slope were controlled by two weirs, one at the downstream end of each of the bifurcate channels. The water plunged over the control weirs from the bifurcate channels into a reservoir. The flow rate was adjusted until uniform flow conditions were achieved within the system. This was achieved by equalizing the water depths in the inlet channel and downstream distributaries just upstream and downstream of the bifurcation, respectively.

A total of eight experiments were performed (Table 1), varying three parameters: width-to-depth ratio (WDR), discharge ratio (Qr), and bed roughness. Experiments were conducted with two different WDRs namely 6.3 and 14.3, the latter representing conditions found in natural systems such as the Cumberland Marshes, Canada [*Edmonds and Slingerland*, 2008] and the Columbia River, Canada [*Kleinhans et al.*, 2012]. For these ratios, water depths of 80 and 35 mm were used, abbreviated as 80xxx and 35xxx herein. Both equal (nnEQ) and unequal (nnNEQ) discharge divisions were examined; discharge ratios of $Qr = 1$ and about $Qr = 1.5$ were used. Downstream weirs were used to control discharge ratio and water depth in each bifurcate. For the equal discharge division runs, discharge and weir heights were adjusted to acquire the required water depth and uniform flow conditions. Experiments with unequal discharge division were always run with the same discharge as their equal counterparts; in these runs uniform flow was acquired by varying weir heights. The backwater adaptation length [*Ribberink and Van Der Sande*, 1985; *Parker*, 2004 also see *Kleinhans et al.*, 2013, for importance in bifurcations, sometimes named backwater length or backwater effect], estimated by $\lambda_{bw}=h/3S$ (h is water depth, S channel slope), equals 27 m for the low width-to-depth ratio, and 12 m for the high width-to-depth ratio experiments. These values are longer than the entire flume, justifying using downstream weirs to control the division of water at the bifurcation. Individual runs were repeated to allow data collection with different techniques.

All the experiments described above were conducted with a smooth bed as well as with a rough bed; experiments with a rough bed are indicated with the suffix _S for sediment. For the experiments with a

Table 2. UDVP Settings and Parameters[a]

	x	y Up	y Down	z
Sample bins	64	64	64	64
First sample distance (mm)	4.995	4.995	4.995	4.995
Sample length (mm)	194.4	496.5	247.6	99.7
Sample distance (mm)	2.96	7.68	3.79	1.48
Sample width (mm)	2.96	2.96	2.96	2.96
Sampling period (ms)	8	8	8	16
Intra-sample delay (ms)	15	15	15	15
Number of probes in cycle	7	7	7	8
Sampling frequency (Hz)	6.21	6.21	6.21	4.03
Maximum depth, L_{max} (mm)	228.29	912.79	912.79	983.46
Min U (mm/s)	0.00	−74.99	−74.99	−69.60
Max U (mm/s)	299.84	74.99	74.99	69.60
Velocity resolution ΔU (mm/s)	1.17	0.59	0.59	0.54

[a]For streamwise (x), cross stream in upstream channel (y up), cross stream in downstream channels (y down), and vertical (z) velocities.

rough bed, a 15 mm thick immobile layer of 3–8 mm ($D_{50} = 5$ mm) white gravel was installed at the bed of the model. The same water depths and discharge ratios were used for the runs with sediment; water levels were measured relative to the top of the gravel bed to retain the same width-to-depth ratio. To ensure uniform flow, but to retain the same WDR, experiments 35EQ_S and 35NEQ_S and experiments 80EQ_S and 80NEQ_S were run at about 60% and 80% of the discharge of their smooth-bed counterparts, respectively. This reduced discharge is caused by slower flow induced by the increased roughness.

2.2. Data Acquisition
2.2.1. Flow Velocity Vectors (UDVP)
A series of measurements were taken from a total of four cross sections distributed throughout the model domain (Figure 1c). 1-D flow velocities were measured sequentially in the streamwise Ux, cross-stream Uy and vertical Uz directions at each cross section (Figure 1c) using an ultrasonic Doppler velocity profiling (UDVP) system [Takeda, 1991, 1995]. A Met-Flow UVP-XW ultrasonic velocity profiler was used to record a multiplexed signal from an array of 4 MHz ultrasonic transducers. The locations of the measurements were chosen such that the individual signals could be combined into time-averaged 3-D flow velocity vectors for each cross section. The positions of the transducers are described in detail in the following paragraphs (also see Figure 1d).

For the measurement of both Ux and Uy, seven UDVP transducers were used. These transducers were placed at a distance of 10 mm from each other. For the lower WDR runs (runs 80xxx), all seven transducers were used to measure flow velocities. For the higher WDR runs (runs 35xxx), only three transducers were submerged due to the shallower water depth. For the measurement of cross-stream velocities, the transducers were mounted on the outside of the Perspex flume wall and sounded the flow using acoustic coupling gel to prevent distortion of the acoustic signal through the flume walls. In the upstream section, the cross-stream measurements were repeated from both sides. Streamwise velocities were measured by inserting the stack of probes in the flow 100 mm downstream of the actual position of the cross section in order to minimize the influence of the probe on the measured flow field. Measurements for Ux were taken at 16 locations per cross section in the upstream channel (see Figure 1d) and at eight locations per cross section in the bifurcate channels (effectively splitting the measurement location shown in Figure 1d). For the measurement of Uz, 16 UDVP transducers were used in the upstream channel and 8 in the bifurcate channels. Transducers were mounted to be only slightly submerged. Locations corresponded with the location of Ux measurements.

The measured streamwise flow velocities Ux were in the range of 40–240 mm/s for the low-WDR runs and 10–200 mm/s for the high-WDR runs. The majority of cross-stream flow velocities Uy were in the range of −10 to +10 mm/s for the low-WDR runs and −5 to +5 mm/s for the high-WDR runs. Vertical flow velocities Uz were in the range of −4 to +4 mm/s for the low-WDR runs and −1 to 1 mm/s for the high-WDR runs. These fell well within the measurable range (Table 2), Ux and Uy were high compared to the flow velocity resolution. Values for Uz come quite close to the minimum measurable value in the high-WDR runs.

For every measurement location, a total of 512 samples were collected. This value was determined using a method to estimate the optimal record length for turbulent flow [*Buffin-Bélanger and Roy*, 2005]. This was achieved via analysis of convergence of the measured velocity to a mean value. Each transducer was set to record 1-D velocities in a profile at 64 distances from the probe. These profiles spanned different lengths for the different measurement orientations and locations: 596.5 mm for cross-stream measurements in the upstream channel, 247.6 mm for cross-stream measurements in the downstream channels, 194.4 mm for streamwise measurements and 99.7 mm for vertical measurements (see Table 2 for full set of properties). For the cross sections in the upstream channel, the cross-stream velocity was measured sequentially from both sides of the channel. At every vector location in each section, the two available values for the cross-stream component taken from either side were compared. If the difference of the two values was within one standard deviation of all cross-stream values, the mean of these values was used. Otherwise, the value with highest magnitude was used. This procedure was followed because in the cross-stream data, vertical bands with zero flow velocities were present in some of the data. It is likely that acoustic reflections from the opposite flume wall induced negative interference and caused these bands.

2.2.2. Near-Bed and Surface Flow Fields (Particle Image Velocimetry)

For all model runs, Particle Image Velocimetry (PIV) [see *Adrian*, 1991, 2005] was used to record 2-D near-surface flow velocity vectors in the streamwise Ux and cross-stream Uy directions. This was achieved through introduction of about 15,000 floating particles ($\rho_s = 660$ kg/m^3, $d = 2.0-2.5$ mm). Additionally, for runs with a smooth bed, near-bed velocities were also measured using PIV using about 10,000 denser ($\rho_s = 1360$ kg/m^3, $d = 2.5$ mm) particles. In contrast to classic PIV techniques with neutrally buoyant small particles and laser sheets, we applied PIV methods to slightly larger floating surface particles and sinking particles at the channel bed [cf. *Jodeau et al.*, 2008; *Blanckaert et al.*, 2013]. Note that the PIV data were collected in separate, repeated runs and not simultaneously with the UDVP data.

For both the near-surface and near-bed measurements, PIV involved uniformly feeding black particles into the inlet channel over a period of about 10 s. A digital SLR camera with High Definition (HD) video capabilities (Canon EOS 550D) with a low-distortion wide angle lens (Canon EF-S 10–22 mm at 20 mm) was used to record the movement of the particles during the run. The camera was mounted perpendicular to the flume in the center of the channel just upstream of the bifurcation head (Figure 1c). The camera was set to shoot HD video (1080 $\times$ 1920 at 29.97 fps). Three 500 W halogen lamps, shielded to prevent reflections at the water surface, illuminated the measurement section. Single frames were extracted from 15 to 20 s of video from each run, resulting in 450–700 individual frames.

For all runs, images of different water levels were used to create image masks to remove areas outside the actual flow field. These masks represent the width of the flume for the different water levels, and effectively correct for vertical relief-displacement. Since the water surface had a low gradient, the camera was horizontal and centered above the flume, and its lens introduced minimal distortion, correction of barrel or perspective distortion was not necessary. Perspective distortion was most significant at the edges of frames, where the angle of incidence was most oblique, but it was minimal directly beneath the camera, which covered the region surrounding the bifurcation. A rectangular region centered on the inlet channel with the bifurcation head as a fixed point was cropped out of the masked image. The resulting image was converted to 8-bit gray scale, inverted and a pixel value threshold was then applied to remove irregularities introduced by the bed and walls. Lighting irregularities were minimal relative to the high contrast between the black particles and white background.

For every pair of consecutive images, flow velocities were calculated using the Mean Quadratic Difference method. This method was chosen as it gives better results in recordings with a high particle density [*Gui and Merzkirch*, 1996; *Merzkirch and Gui*, 2000]. Velocity vectors were calculated in MATLAB using a bespoke toolbox [based upon *Mori and Chang*, 2003] using sampling windows of 32 $\times$ 32 pixels. This method uses a subpixel estimate of particle location based on pixel values. The pixel size is about 0.5 mm which, with a 30 fps frame rate, yields a theoretical minimum velocity resolution of 0.05 mm/s. Vectors were spaced such that each data set contains 32 vectors per channel width, which corresponds to a vector spacing of 32 pixels for the low-WDR runs (80xxx) and 30 pixels for the high-WDR runs (35xxx, Table 1), resulting in overlap of 1 pixel at each side of the sampling window in the high-WDR runs. The magnitude of the vectors was corrected for the different field of views for the different water heights. Filtering was applied to the velocity time series at every vector location, resulting in all spurious vectors outside a range of 2 standard deviations

from the local mean being removed from the data set. This filtering resulted in the removal of about 10% of the vectors in the surface measurements for the smooth-bed runs and about 35% of the rough-bed runs. For the near-bed measurements of the smooth-bed runs, about 5% of the vectors were filtered. The quality of this method seems to be related to artifacts introduced by visible shadows caused by the gravel in the setup. The mean values per time series were used in further analysis. Note that no spatial filtering or any form of interpolation was performed on the data.

2.3. Data Analysis
2.3.1. Discharge and (Depth-) Averaged Velocities

The measured UDVP data were used to calculate cross-sectional discharge and average flow velocity vectors. The average flow velocity was calculated for each measured cross-section cs and at each measured depth profile y. The cross-sectional discharge Q_{cs} (m³/s) was calculated by summing the products of streamwise flow velocity measurements Ux (m/s) and their effective area a (m²):

$$Q_{cs} = \sum_{y=1}^{n_y} \sum_{z=1}^{n_z} \left(Ux_{y,z} \cdot a_{y,z} \right) \tag{1}$$

where n_y and n_z are the number of depth profiles and vertical locations in each profile, respectively. a is calculated from the distances from the centers between measurement locations or the flow boundaries at the outer edges. The cross-sectional averaged velocity $U_{av,cs}$ (m/s) is the discharge through that cross section (Q_{cs}) divided by cross-sectional area $A = W \cdot H$ (m²):

$$U_{av,cs} = Q_{cs}/A \tag{2}$$

The discharge passing through the upstream sections CS01, CS02, and CS03, and the summed discharge of both downstream sections CS04L and CS04R were evaluated for continuity by calculating the root-mean-square (RMS) deviation from the mean discharge $\bar{Q}$ of all four sections:

$$Q_{rms} = \sqrt{\frac{1}{n} \sum_{cs=1}^{n} \left(\bar{Q} - Q_{cs} \right)^2} \tag{3}$$

where n is the number of measured cross sections. At each measured vertical profile y, the discharge per unit width qx_y (m/s) was calculated in a similar way as the cross-sectional discharge:

$$qx_y = \sum_{z=1}^{n_z} \left(Ux_{y,z} \cdot h_z \right) \tag{4}$$

where h_z is the effective height of each measurement. For the depth-averaged flow velocity vectors $Ux_{av,y}$, the discharge per unit width qx_y was divided by the flow depth H:

$$Ux_{av,y} = qx_y/H \tag{5}$$

Equations (4) and (5) were also applied to attain depth-averaged cross-stream flow velocities $Uy_{av,y}$ by substituting streamwise flow velocities Ux by cross-stream flow velocities Uy.

2.3.2. Streamwise Circulation and Planar Vorticity

UDVP measurements were used to calculate the streamwise circulation at each cross section. PIV data were used to calculate the planar vorticity field for both the surface and the near-bed measurements.

The streamwise circulation Γ of a flow is a measure of the amount of rotating fluid in a cross section. This circulation is calculated by taking the area integral of the two-dimensional vorticity (ω, in the y-z plane) per cross section:

$$\Gamma = \int_z \int_y \omega \, dy \, dz \tag{6}$$

where Γ (m^2/s) is the circulation and ω (rad/s) is the vorticity, which is defined as the curl of the vector velocity field:

$$\omega = \nabla \times \vec{\mathbf{u}} \tag{7}$$

where $\vec{\mathbf{u}}$ is the 2-D vector field of cross-stream and vertical flow velocities Uy and Uz from UDVP measurements.

In order to compare the circulation for different cross sections, the circulation is computed using the absolute values of the vorticity ($\omega = |\omega|$ in equation (6)). The vorticity is normalized using the method of *van Balen* [2010, p. 77]:

$$|\hat{\Gamma}| = |\omega| H / (A \cdot U_{av,cs}) \tag{8}$$

where $|\hat{\Gamma}|$ is the absolute normalized circulation.

Details of the secondary flow structure are also shown by the planar vorticity (in the *x-y* plane) using equation (7), but using cross-stream flow velocities (Uy) and downstream flow velocities (Ux) for vector field $\vec{\mathbf{u}}$, taken from PIV measurements of the surface flow and near-bed flow.

2.4. Data Quality
2.4.1. Development of Turbulence
We analyzed the UDVP data at CS01 to ascertain whether the flow was fully turbulent. Turbulent flow conditions result in a logarithmic velocity profile. We tested if such profile existed in the measured flow velocities. At each vertical profile *y*, we applied a logarithmic regression to predict the streamwise flow velocity $\hat{U}x$ as a function of the height above the bed *z*:

$$\hat{U}x(\log(z)) = a_0 + a_1 \log(z) \tag{9}$$

where a_0 and a_1 are linear regression coefficients. We analyzed these profiles visually and we indicate how good the data fits the model with the coefficient of determination R^2, which is calculated as:

$$R^2 = 1 - \frac{\sum \left(Ux(z) - \hat{U}x(z)\right)^2}{\sum \left(Ux(z) - \overline{Ux}\right)^2} \tag{10}$$

where $\overline{Ux}$ is the average flow velocity in the profile under consideration.

2.4.2. Scaling Assessment
We used the Froude number, Reynolds number, and Weber number to evaluate the hydraulic behavior of our experiments. We evaluated these values from UDVP measurements in the upstream section of the experiment. The Froude number (*Fr*) determines whether the flow is affected by downstream or upstream disturbances, respectively, subcritical (*Fr* < 1) or supercritical (*Fr* > 1) flow. Subcritical flow conditions are desirable.

$$Fr = \frac{U}{\sqrt{gH}} \tag{11}$$

where *g* is the gravitational acceleration (9.81 m/s^2). The Reynolds number (*Re*) indicates if the flow is turbulent (*Re* > 2000) or laminar (*Re* < 500), with a transitional region in between:

$$Re = \frac{UR}{v} \qquad (12)$$

where R is the hydraulic radius (m), $R = (H \cdot W)/(2H + W)$, v is the kinematic viscosity of water (m²/s), $v \approx 4 \times 10^{-5}/(20 + t)$, where t is the temperature (18°C for the current experiments). We aimed for turbulent flow in our experiments.

Weber (number We) shows the relation between inertia and surface tension forces [*Peakall and Warburton*, 1996]. Critical values for the Weber number are uncertain and vary from 10 to 100, so we aim for values above this range.

$$We = \frac{U^2 \rho H}{\sigma} \qquad (13)$$

where ρ is the density of water and σ is the surface tension. We used an estimate of $\sigma = 6 \times 10^{-3}$ N/m in our experiments as opposed to the value of 7×10^{-2} N/m for water because we added soap in the water to reduce the surface tension.

3. Results

3.1. General Flow Structure

The following key flow field properties were derived from UDVP data (Table 1): (1) all equal weir runs had equal (50/50) discharge division; (2) all unequal weir runs had a discharge division close to 40/60. The measured discharge was less uniform for the shallower runs with a rough bed (Table 1, Q_{RMS}), which is probably due to the higher levels of noise present in the UDVP measurements for these runs.

3.2. Effect of Flow Division on Flow Structure

In the low-WDR smooth-bed runs with equal discharge division (Run 80EQ), the high velocity core was positioned in the center of the channel (Figure 2). In the unequal discharge division case (80NEQ), the flow velocity core was located to the right-hand side in the two downstream cross sections (Figure 3), the side with the gradient advantage and largest discharge. In both the equal and unequal cases (80EQ, 80NEQ), two opposed secondary flow cells were present in the channel upstream of the bifurcation. These cells flowed toward the center of the channel at bed level and toward the banks at the water surface (Figures 2a, 2b and 3a, 3b). However, in the unequal discharge division case, the cell at the side of the channel with the highest discharge was smaller (Figures 3a and 3b). In both cases, the division of flow becomes visible in CS02 and dominates the flow structure in CS3. In the latter, the rotational flow cells are almost absent (Figures 2c and 3c). For a large portion of the width (about 80%) in the unequal discharge division case, the flow structure caused the near-bed velocities to be oriented toward the channel with the water surface gradient advantage (Figures 3c and 4b). Note that a flow direction toward the right channel does not mean that this flow indeed enters the right channel, as we will discuss later.

In both bifurcate channels, most velocity vectors were consistently directed toward the inner bank while the near-bed vectors were directed toward the outer banks (Figures 2d, 2e and 3d, 3e). This flow structure had an inverse direction of rotation compared to the flow cells upstream of the bifurcation.

The PIV vectors obtained for the near-surface and near-bed flow reveal a more detailed flow field in the horizontal plane than the UDVP data (Figures 5 and 6), especially in the area just upstream of the bifurcation (the downstream-most UDVP section (CS03) is located at $x = 431$ mm in Figures 5 and 6). In this zone, the flow divergence and steering into the bifurcate channels becomes even stronger than at the locations observed with UDVP data (Figure 5). Moreover, near-bed flow accelerates closer to the bifurcation (Figures 6b and 6d). Indeed, just upstream of the bifurcation ($x = 550$ mm, Figure 6) the near-bed velocity vectors were almost perpendicular to the outer banks in both cases with unequal discharge division (nnNEQ).

Flow division lines (Figure 7) were derived from the near-surface (Figure 5) and near-bed velocity vectors (Figure 6). These lines indicate the spatial location of the division of incoming near-surface and near-bed fluid into the two bifurcate channels. Important observations from these divisions include: (1) in symmetrical bifurcations both the discharge ratio, Q_{right}/Q_{total}, and the near-bed division ratio, $q_{bed,right}/q_{bed,total}$, were about 50%; (2) in asymmetrical bifurcations $q_{bed,right}/q_{bed,total}$ (71%) was much greater than Q_{right}/Q_{total} (62%)
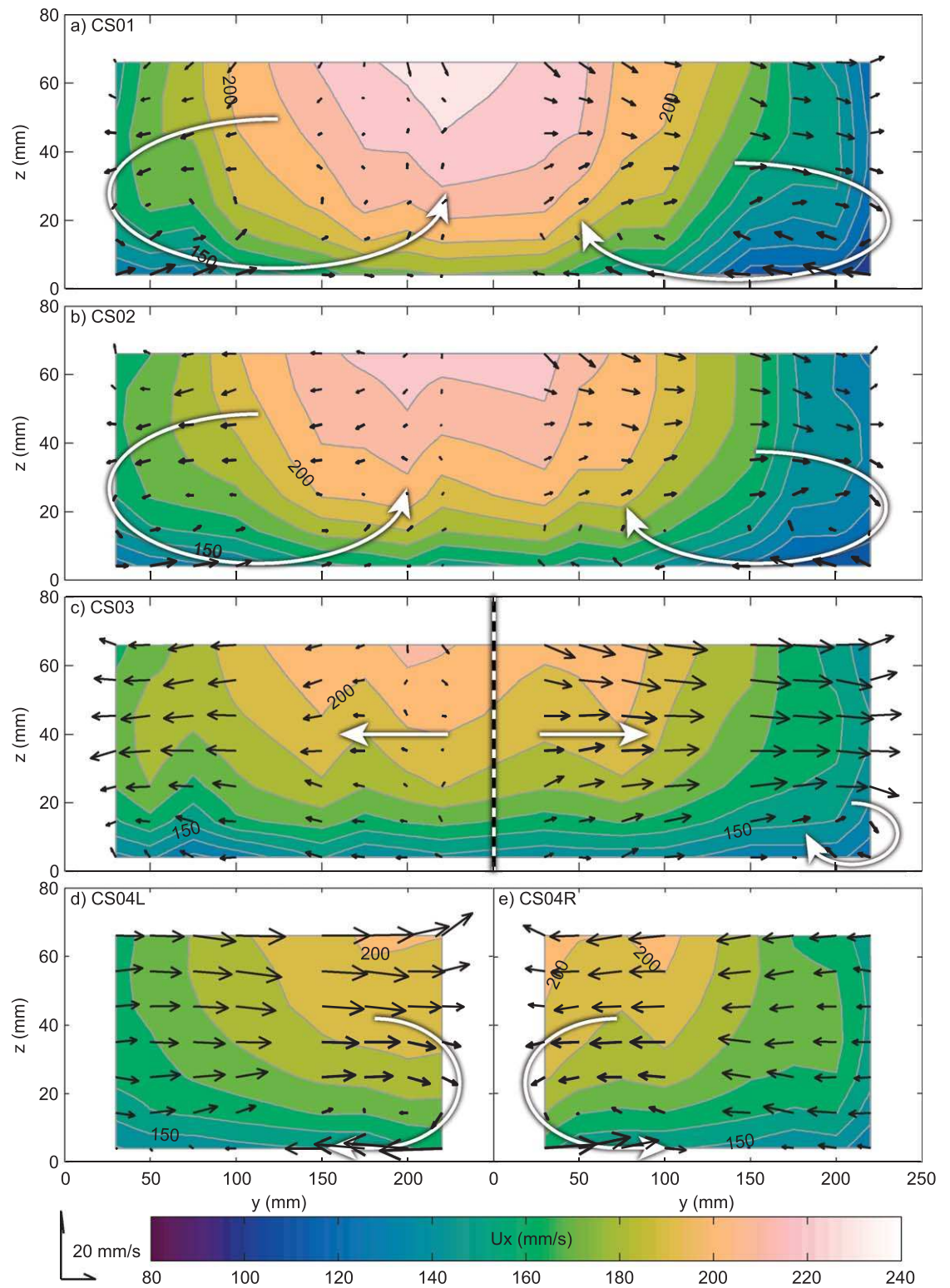
Figure 2. 3-D velocity components (UDVP data) for run 80EQ, at cross sections (a) CS01, (b) CS02, (c) CS03, (d) CS04L, and (e) CS04R. Color contours show streamwise velocity (Ux), black arrows show cross stream (Uy) and vertical (Uz) velocity components, white arrows indicate the bulk flow structure, and dashed line shows the approximate location of flow division ($Uy = 0$). Axis orientation is such that the "flow goes into the paper"/looking downstream. Vertical axis and vertical flow velocities are 2 times exaggerated with respect to cross-stream axis and flow velocity.
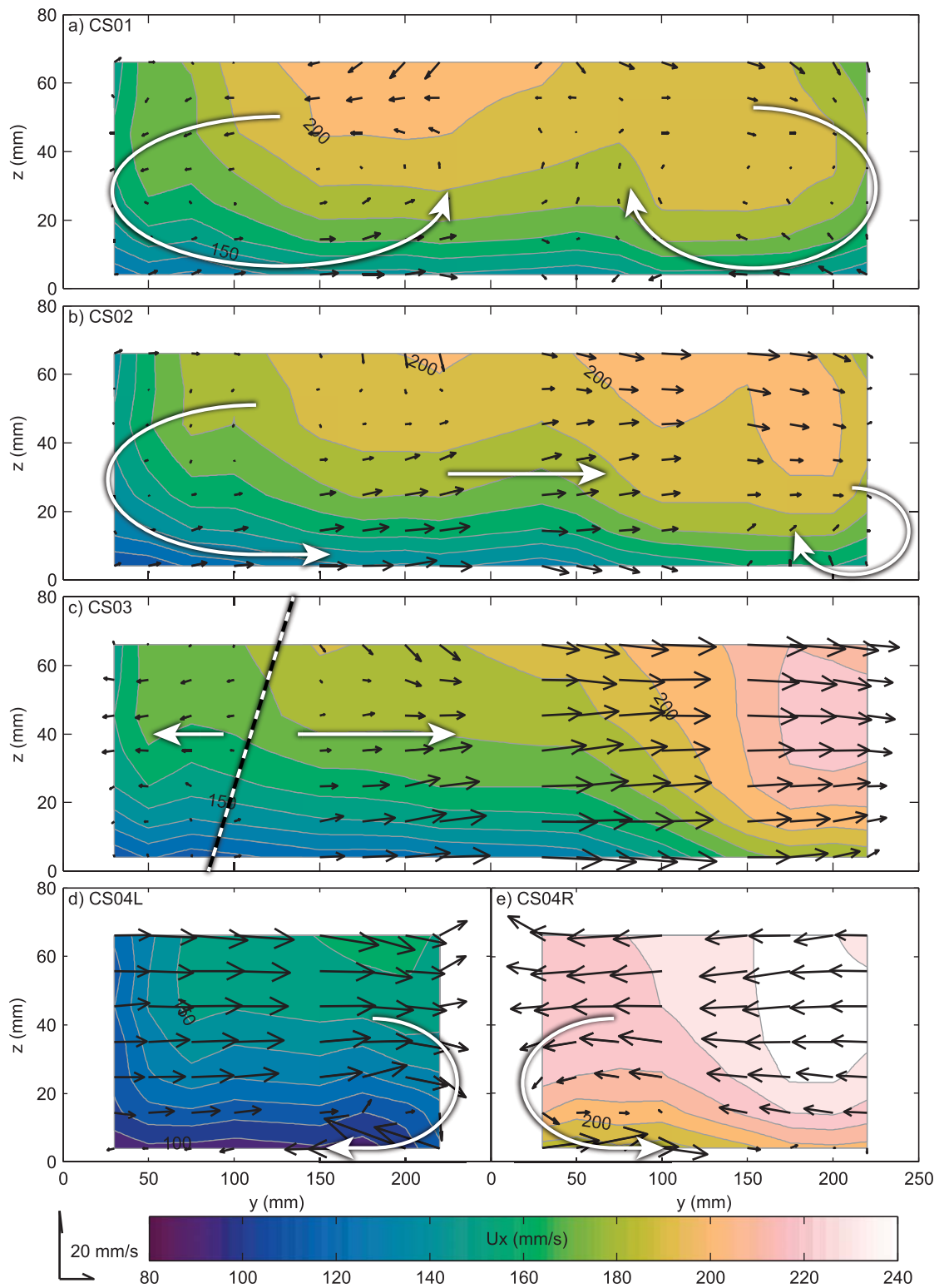
Figure 3. 3-D velocity components (UDVP data) for run 80NEQ, see Figure 2 for caption.
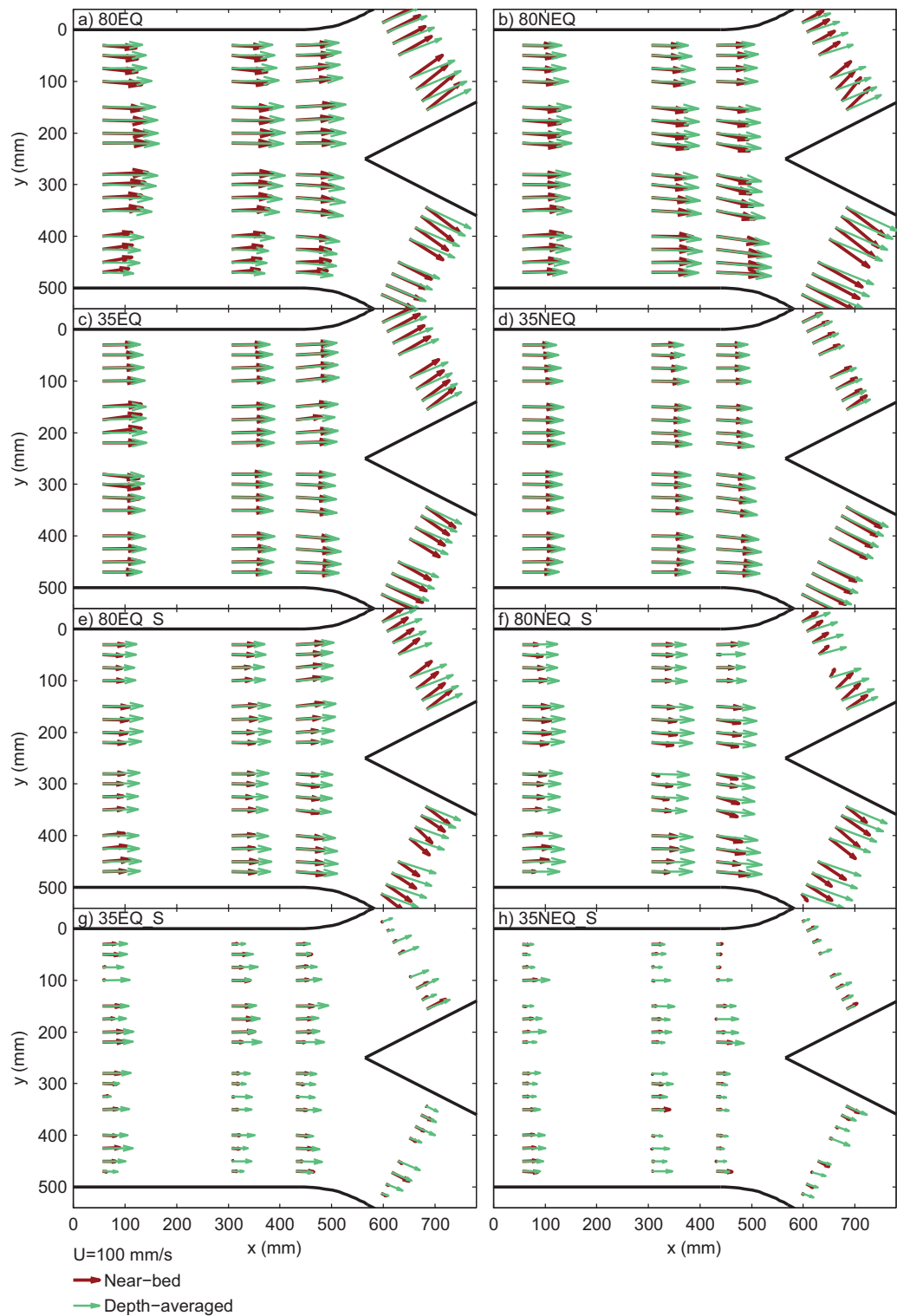
Figure 4. Depth-averaged (DA, light-green) and near-bed (NB, dark-red) flow velocity vectors (UDVP data) at all measured cross sections. Axis labels were removed where they are the same as the adjacent graphs. Secondary flow structures caused the direction of the near-bed flow to deviate from the depth-averaged flow. This effect was more pronounced in the low WDR, asymmetrical runs (80NEQ/80NEQ_S). The high WDR, rough bed runs are noisy due to acoustic resonance in the flume.
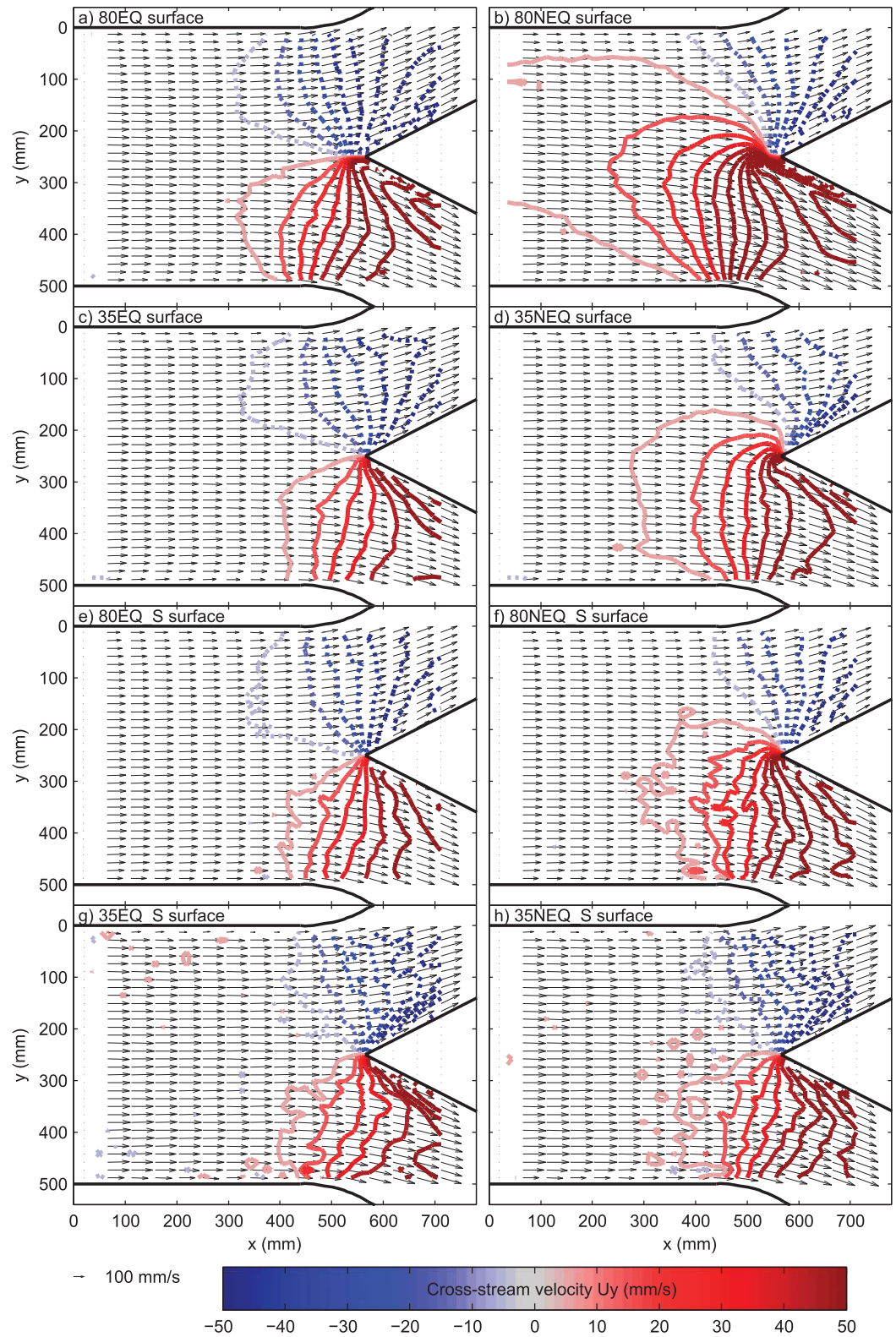
Figure 5. Near-surface velocity vectors (PIV data, arrows). Cross-stream flow velocities are emphasized with colored contours, which indicate the magnitude of cross-stream flow *Uy* relative to the orientation of the walls of the upstream channel. Red contours indicate flow to the right, blue/dashed contours indicate flow to the left, first contour = 5 mm/s, contour interval = 10 mm/s. For clarity, only every third vector in the downstream direction is shown.
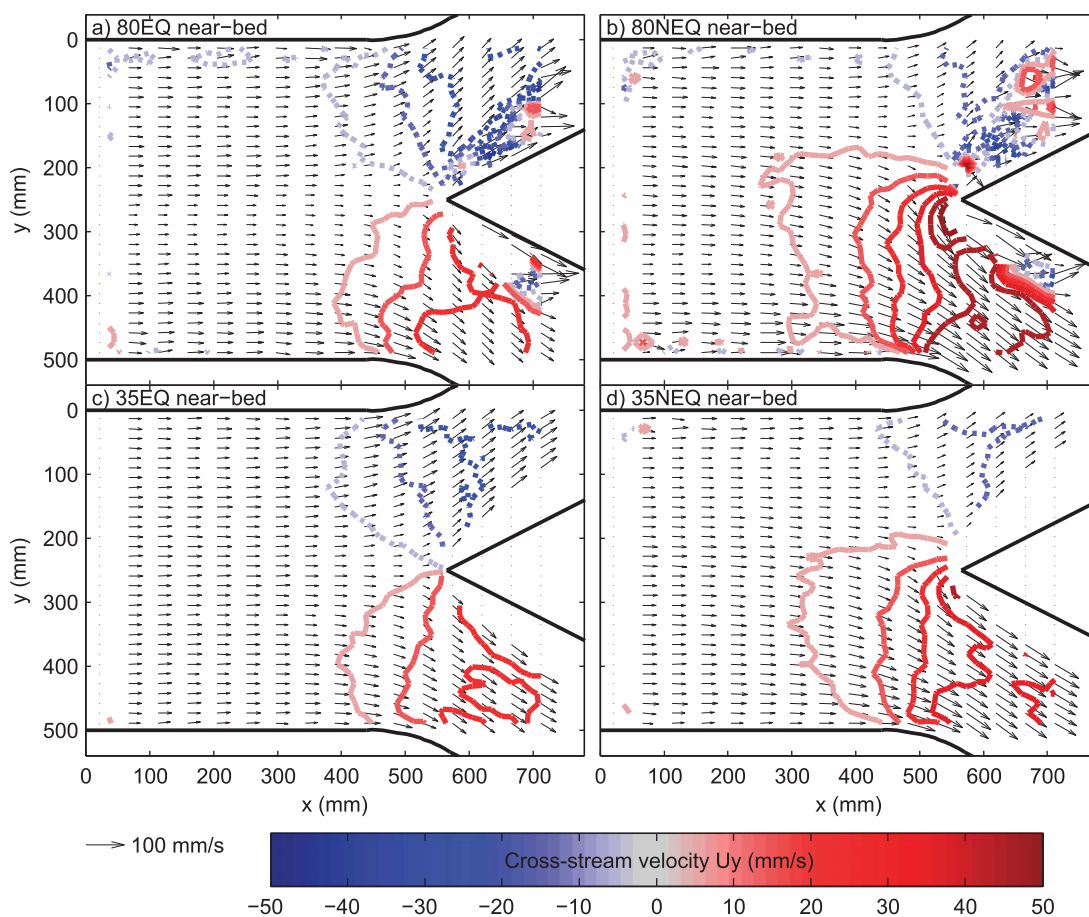
Figure 6. Near-bed velocity vectors (PIV data, arrows), see Figure 5 for caption.

(Table 1); and (3) the majority of this division of near-bed flow occurred within a distance of about one channel width upstream of the bifurcation (Figure 7b).

3.3. Effect of Width-to-Depth Ratio on Flow Structure

Similar flow features described above were also observed in the higher WDR runs 35EQ and 35NEQ (see Figures 8, 9 and 4c, 4d), although some differences exist. There is no high flow velocity core in the middle of the channel, but the highest flow velocities are spread over a larger part of the channel (Figure 8c). Moreover, there are two locations with higher velocities, one in the left and one in right part of the upstream channel, which align with the highest velocity cores in the bifurcate channels (Figures 8d and 8e). Also, in the unequal discharge case, the streamwise velocities develop toward one core of flow velocity on the side of the channel with the largest discharge (Figure 9c). The secondary flow structures upstream of the bifurcation consist of two counter-rotating flow cells in the middle of the channel flowing toward the banks near the bed (Figure 8a). Additionally, a third and fourth flow cell was present near the banks, with flow directed toward the banks near the water surface (Figure 8a).

The secondary flow structure at the center of the channel in the high-WDR runs mirrored that observed in the low-WDR runs. In addition, downstream of the bifurcation, the secondary cells did not change their sense of rotation and instead continued to rotate in the same orientation as upstream of the bifurcation, with upwelling at the location of the highest streamwise velocity. These flow cells were not observed upstream of the bifurcation in the unequal discharge division high-WDR run 35NEQ (Figure 9). We speculate that the divergence close to the bifurcation and the flow cells within the bifurcate channels are comparable to the structure observed in the low-WDR runs and suppress the flow cells closer toward the bifurcation (Figures 8b and 8c). Note that the orientation of the secondary flow structures was largely inferred from the
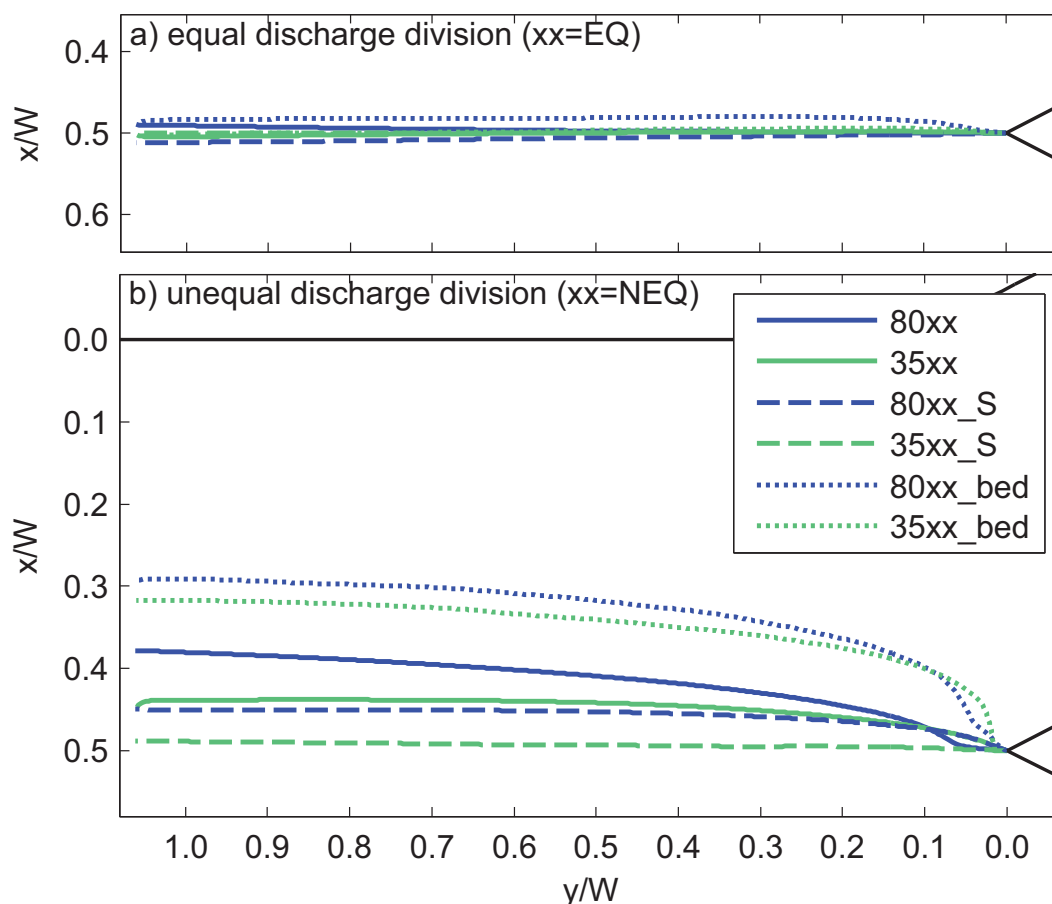
Figure 7. Division of flow at the bifurcation derived from PIV flow fields. (a) Equal discharge division runs (read legend as xx = EQ), and (b) unequal discharge division runs (read legend as xx = NEQ). Solid black lines show the boundaries of the bifurcation model. Solid lines denote the division between surface water entering the left and right channels for the smooth-bed runs, dashed lines show the surface water division for the rough bed runs. Dotted lines denote the division of incoming near-bed flow between the left and right channels.

cross-stream velocities because the vertical velocities were close to or less than the measurement resolution.

There was no clear difference in the direction of near-bed and depth-averaged flow (Figure 4). However, a divergence between near-bed and surface water was observed in the zone just upstream of the bifurcation (between $x = 400$ mm and the bifurcation) in both the low-WDR runs (80EQ, 80NEQ, Figures 5a and 5b) and high-WDR runs (35EQ, 35NEQ, Figures 5c and 5d). This diversion extended farther upstream and was significantly more pronounced in the low-WDR runs. The near-surface velocities are affected by the unequal discharge distribution at a distance of about one channel width upstream of the bifurcation in the low-WDR run (80NEQ, Figure 7b) and about half a channel width in the high-WDR run (35NEQ, Figure 7b). Interestingly, the low-WDR has less impact upon near-bed cross-stream flow velocities than on the near-surface flow. This effect is shown in terms of flow division (Figure 7 and Table 1): in the high WDR run (35NEQ), a larger proportion of the near-surface flow enters the bifurcate channel with a gradient advantage ($q_{surf,right}/q_{surf,total}$=62%) whereas in the low-WDR run this is somewhat lower ($q_{surf,right}/q_{surf,total}$=56%). The same holds for near-bed flow, but with a smaller difference observed between the two runs ($q_{bed,right}/q_{bed,total}$=71% and $q_{bed,right}/q_{bed,total}$=68% for runs 80NEQ and 35NEQ, respectively).

3.4. Flow Circulation

Upstream of the bifurcation, there were two counter-rotating flow cells with upwelling flow in the middle of the channel in the low-WDR runs. These cells were symmetrical in the symmetrical bifurcation (Figure 2a) and were unequal in size in the asymmetrical bifurcation (Figure 3b). In the high-WDR runs, two counter-rotating flow cells with downward flow in the middle and two weaker flow cells with downward flow near
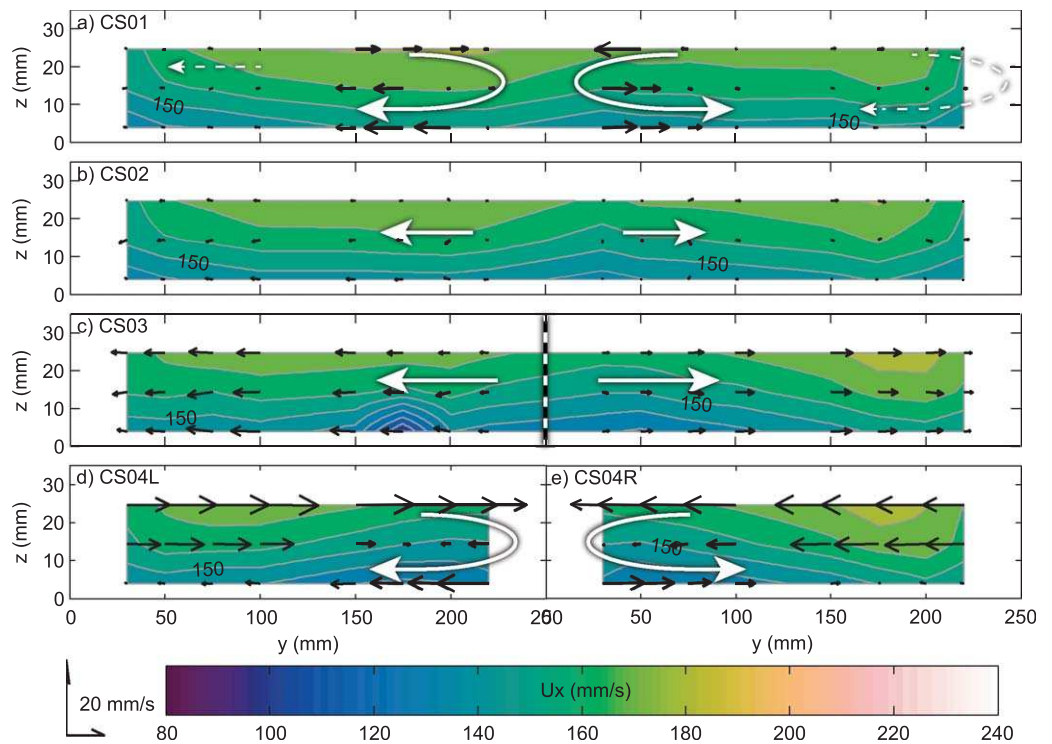
Figure 8. 3-D velocity components (UDVP data) for run 35EQ, see Figure 2 for caption.
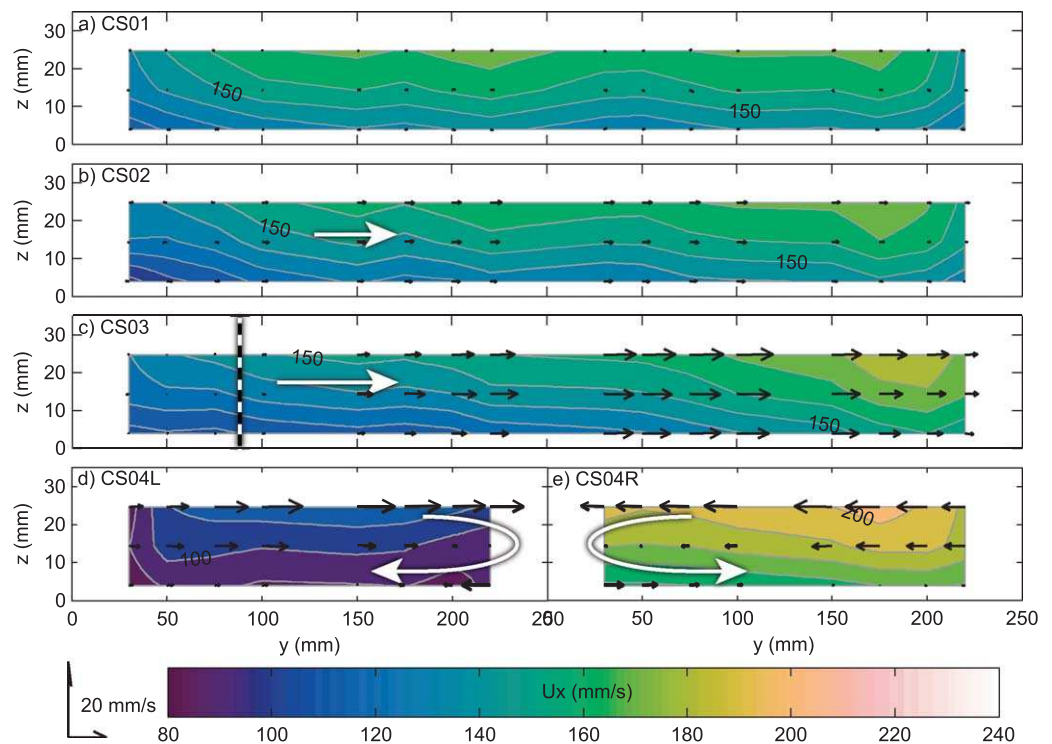

Figure 9. 3-D velocity components (UDVP data) for run 35NEQ, see Figure 2 for caption.
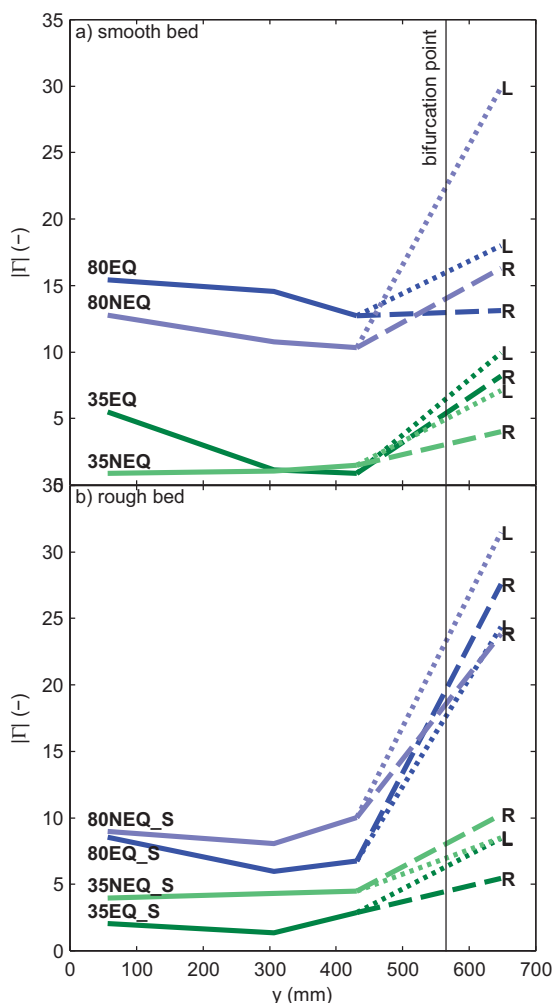
Figure 10. Absolute normalized circulation derived from UDVP data for all (a) smooth-bed runs and (b) rough bed runs plotted against downstream coordinate y. For the most downstream location, the lines split for the left and right bifurcate channel. Blue lines represent the low-WDR runs, green the high-WDR runs. Dark colors represent equal discharge division runs, pale colors the unequal discharge division runs.

the banks on either side were observed in the symmetrical run (Figure 8a), but this structure was not observed in the unequal discharge run (Figure 9a). In all cases, these flow cells were suppressed by strong divergence closer to the bifurcation. Downstream of the bifurcation, a single flow cell was present in each bifurcate channel with flow toward the outer bank near the channel bed (Figures 2d, 2e, 3d, 3e, 8d, 8e, and 9d, 9e). The magnitude of circulation consistently increased downstream of the bifurcation in all runs (Figure 10). Earlier results [*Thomas et al.*, 2011] already show the inversion of direction and increase in magnitude of flow rotation in the bifurcate channel. This effect is attributed to super-elevation of the water surface at the bifurcation point.

The low-WDR runs (80xx) had a higher relative circulation than the high WDR runs (35xx) (Figure 10). For unequal discharge division cases, the subordinate left channel (gradient disadvantage and thus lower discharge) had a 20–50% larger intensity of normalized circulation than the dominant right channel (Figure 10). In the equal discharge division cases, there were differences in circulation between the bifurcate channel, but these were small and not always stronger in the same channel (Figure 10). Perhaps the most notable difference was for 80NEQ, which is likely to had the strongest transverse flow velocities because of the low-WDR and smooth bed.

The planar vorticity of the near-surface flow field shows the presence of rotating cells in the smooth-bed runs (Figures 11a–11d). The general pattern corresponds with the flow structures observed in the UDVP data, with the presence of two counter-rotating flow cells in the low-WDR runs (Figures 11a and 11b) and the presence of two additional cells in the high-WDR runs (Figures 11c and 11d). The main vorticity pattern in the low-WDR runs corresponds with a high flow velocity core in the middle of the channel and slow flow on the sides, which results in rightward vorticity on the right-hand side of the channel and toward the left on the left-hand side. In the high-WDR runs, there is no concentrated velocity core in the middle of the channel, the high velocity is more spread over a larger area. In this case, the patterns of planar vorticity indicate multiple counter-rotating flow cells. In both cases, the planar vorticity pattern follows the streamline curvature. The pattern of planar vorticity in the near-bed flow (Figure 12) also shows a banded pattern. However, there are more small-scale features. These patterns do not resemble those observed in the surface data. Additionally, these patterns also show dividing and splitting circulation bands.

Spatially averaged vorticity (Figure 13) shows the cross-sectional average planar vorticity pattern in the upstream reach. The large-scale pattern for the low-WDR runs is consistent for both the equal and unequal discharge division and both smooth and rough bed runs (Figure 13a). This pattern is the result of the high-
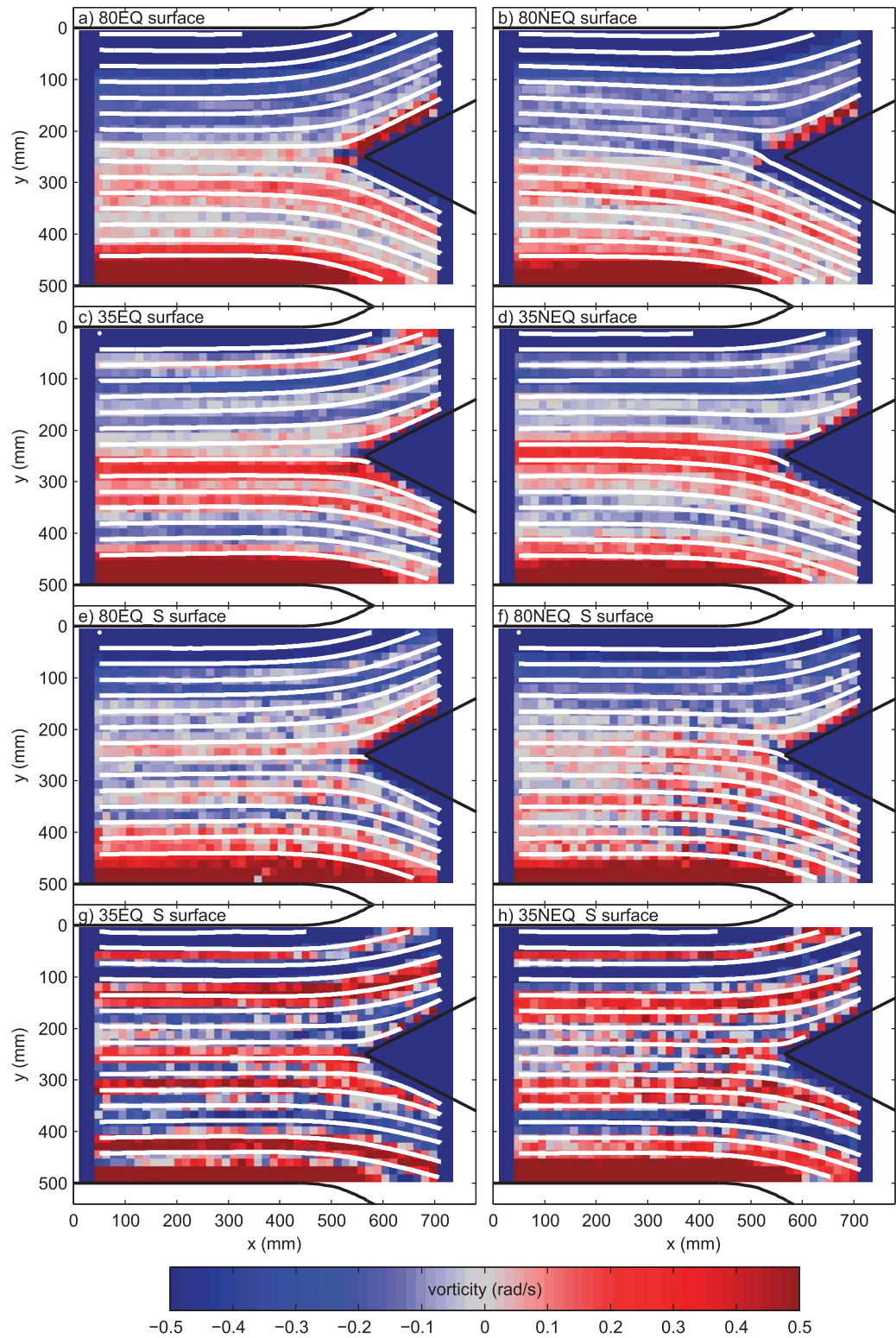
Figure 11. Surface flow vorticity derived from PIV data. Blue indicates counter-clockwise circulation and red indicates clockwise circulation. White lines are streamlines derived from PIV data.

flow velocity core in the center of the upstream channel which curves toward the outer banks and is consistent with the flow structures observed in the cross section. The vorticity pattern in the high-WDR runs shows local vorticity patterns superimposed on a large-scale vorticity pattern (Figure 13b). This pattern is
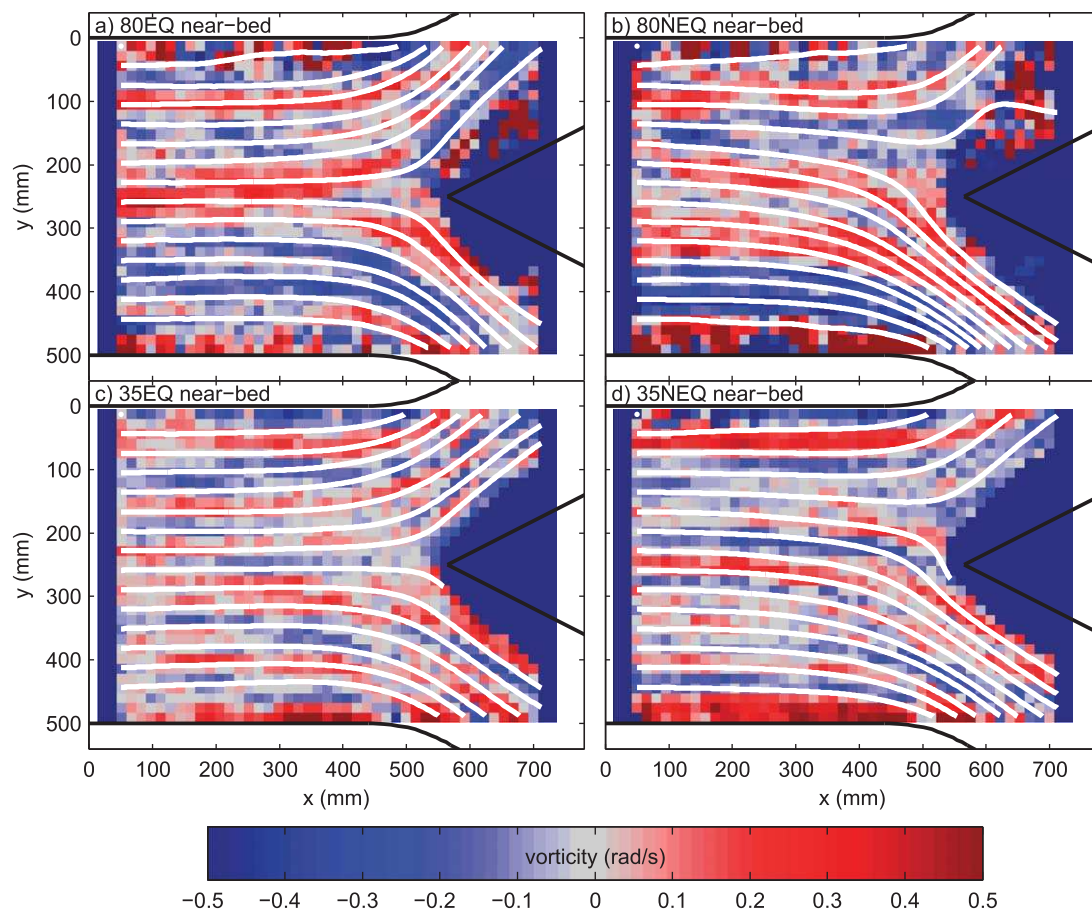
Figure 12. Near-bed flow vorticity derived from PIV data. See Figure 11 for caption.

consistent with local flow structures, as also observed in cross-section data (Figures 8 and 9). Vorticity of the near-bed flow shows a local pattern without a large-scale structure (Figures 13c and 13d).

3.5. Effect of Bed Roughness on Flow Structure

In the runs with a rough bed (nnxxx_S), the deviations of the near-bed velocity from the depth-averaged velocity in the low-WDR rough bed experiments were similar to their smooth-bed counterparts (Figures 4e and 4f, 80EQ_S, 80NEQ_S). Flow velocities were lower in the rough bed cases. Additionally, the decrease in flow velocity toward the bed is stronger for the rough bed cases. The general flow structures were similar to those in their smooth-bed counterparts but were smaller in magnitude (Figures 5e–5h).

The high WDR, rough bed experiments (Figures 4g and 4h, 35EQ_S, 35NEQ_S) showed significant levels of noise induced by acoustic interference between the rough bed and the UDVP. Unfortunately, the near-bed flow field could not be quantified using PIV because of entrapment of particles in the bed sediment. In the rough bed runs, the upstream influence of the bifurcation extends for only half the distance observed in their smooth-bed counterparts. Near-surface flow is divided more equally between the distributaries (Figure 7 and Table 1, $q_{bed,right}/q_{bed,total}$=55% for run 80NEQ_S) and almost equal in the higher WDR run ($q_{bed,right}/q_{bed,total}$=51% for run 35NEQ_S). Compared to the smooth-bed runs, similar vorticity patterns are visible in the rough bed cases, although these are noisier (Figures 11e–11h). The effect of bed roughness is dependent upon the WDR: in the low-WDR runs, both the smooth and rough beds show similar banding of comparable magnitude (Figure 13a) whereas in the high-WDR runs the rough bed shows similar banding, but at about a 2–4 times higher magnitude (Figure 13b, pale colored lines). This comparison shows that stronger flow structures emerged preferentially in channels with a larger width-to-depth ratio, but were reduced in channels with a larger ratio of roughness length to water depth.
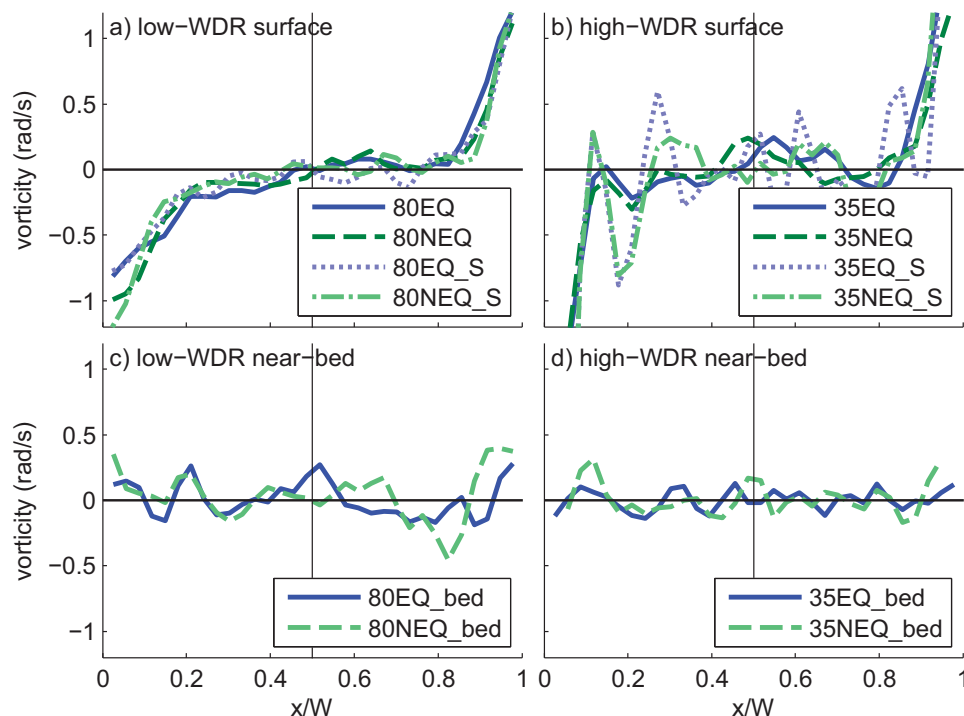
Figure 13. Average vorticity in the upstream part of the bifurcation model ($0 < x < 320$ mm) plotted against normalized channel width (0 = left bank, 1 = right bank) for (a and b) surface flow and (c and d) near-bed flow. Figures 13a and 13c show the low-WDR runs, Figures 13b and 13d show the high-WDR runs.

4. Discussion

4.1. Scaling Assessment and Robustness of Methods

In all experimental runs, the flow was subcritical with Froude numbers between 0.1 and 0.3 (Table 1). The Reynolds number was well above the threshold for turbulent flow ($Re > 2000$) in all low-WDR runs and in the smooth-bed high-WDR runs. Re values for the high-WDR runs with rough bed, equal discharge division (35EQ_S) are closer to, but still above 2000. Run 35NEQ_S had a Reynolds number slightly below 2000 (Table 1). The same is shown by the flow velocity profiles at the most upstream cross section: the measured flow velocity profiles show a well-developed logarithmic profile in all low-WDR runs (Figure 14a) and in the high-WDR, smooth-bed runs (Figure 14b, closed symbols). The high-WDR, rough bed runs show more scattered velocity profiles (Figures 14b and 14c, open squares), which is most probably due to noise in the measurements due to the high amount of acoustic scattering on the rough bed and the limited water depth. Nevertheless, the Reynolds number is in the upper end of the transitional regime and the velocity profiles show no indication of laminar flow so we believe these experiments to have had fully turbulent flow.

Deviations from the logarithmic profile are apparent close to the flume wall (Figure 14a, probe 1). The deviation from a logarithmic profile is visible in all measurements and most prominent in the smooth bed, low-WDR runs (Figure 14c, closed circles). This wall friction effect is expected and is perhaps even more important in natural channels.

In small-scale experiments, surface tension might have an effect on the dominant processes. In our experiments, however, the relative importance of the fluid's inertia to the surface tension is very low as the Weber number is above the critical value of 100 for most runs and well above 10 for the high-WDR, rough bed cases. Note that the reported critical values are not consistent [*Peakall and Warburton*, 1996].

We compared the streamwise velocity from UDVP measurements closest to the water surface to the surface PIV data at the same location (Figure 14d). Note that these two methods do not measure exactly the same flow in terms of time and space. However, the comparison is useful in that it provides a way to see whether
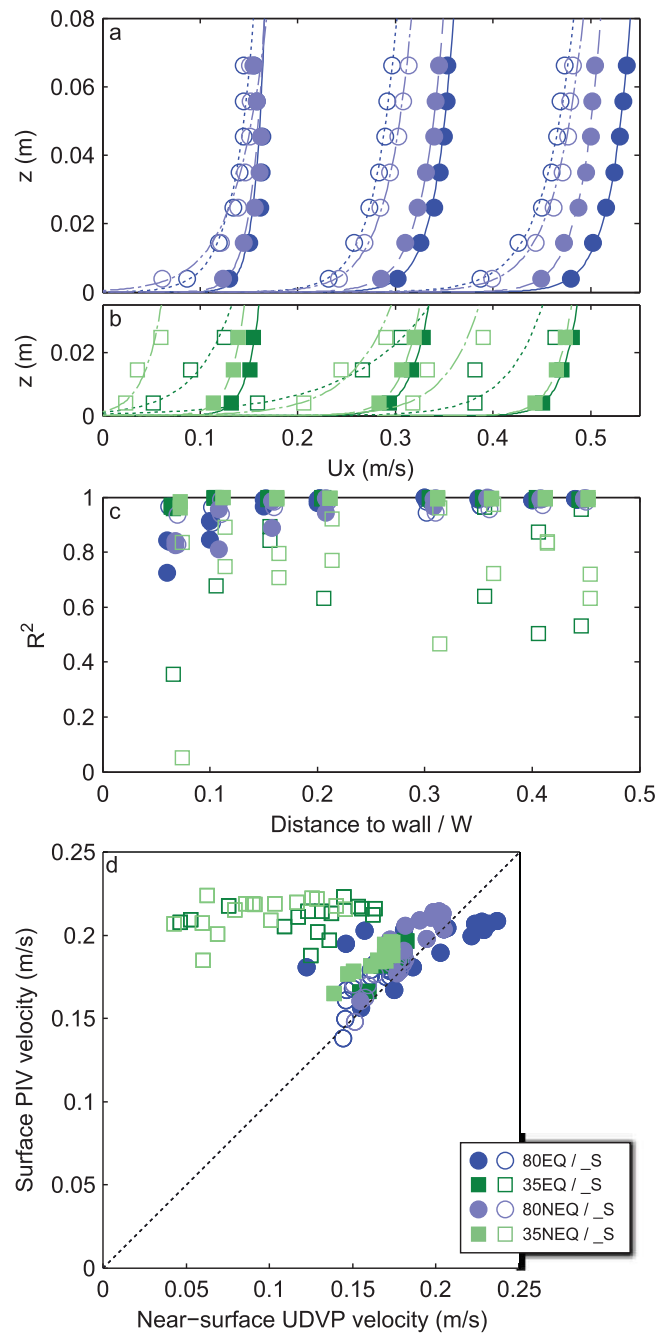
Figure 14. (a and b) Measured streamwise velocity profiles (symbols) and logarithmic fit (lines) at CS01 at probe location 1 (next to wall), 4 and 8 (near-center) for all (a) low-WDR runs and (b) high-WDR runs. The data for Probes 4 and 8 are horizontally offset for visual clarity. Open symbols show the experiments with rough bed, pale colors are the unequal discharge division runs. (c) The coefficient of determination (R^2) of the logarithmic fit of flow velocities for all probes in CS01, shown against normalized distance to the wall, where the flume wall is at 0 and the center of the channel at 0.5. Symbols are plotted with slight horizontal offset for clarity. (d) Measured near-surface streamwise velocity from UDVP data plotted against surface streamwise velocity from PIV data.

there are issues with any of the data. Most measurements are close to being equal, with the majority of PIV data giving slightly higher values, except in the case of the rough bed high-WDR runs where the UDVP data is noisy.

4.2. Implication for Bifurcation Instability

Flow structure at bifurcations is determined by (1) flow forcing by streamline curvature, angular divergence upstream, and through a bifurcation and related zones of flow separation [e.g., *Ramamurthy et al.*, 2007]; (2)

the width-to-depth ratio and flow field inertial and momentum forces [e.g., *Bradbrook et al.*, 2001; *Parsons et al.*, 2007]; (3) flow field super-elevation and related pressure gradient terms [e.g., *Shettar and Keshava Murthy*, 1996]; (4) backwater surface slopes; and (5) topographic forcing by the bed [e.g., *McArdell and Faeh*, 2001; *Bolla Pittaluga et al.*, 2003; *Kleinhans et al.*, 2008]. In this paper, two-independent flow measurement techniques have been used to quantify flow fields in a morphologically symmetrical experimental bifurcation. Flow structures develop that can significantly modify the near-bed flow direction at a distance of up to one channel width upstream of the bifurcation head. The character of the flow was turbulent and highly subcritical with strong backwater effects. Data obtained from control experiments with equal discharge partitioning do not show asymmetric near-bed flow but do have some flow structures that contain counter-rotating transverse-vertical cells upstream of the bifurcation in addition to a clear signal of the bifurcating flow closer to the bifurcation. In the experiments with unequal discharge partitioning, the near-bed transverse flow was directed toward the bifurcate channel which had a gradient advantage and largest discharge. About 80% of the near-bed flow entered the larger channel. Furthermore, as expected, the transverse flow component is larger for channels with larger water depth relative to channel width and relative to the characteristic length of bed roughness. This flow structure upstream of the bifurcation is caused by flow curvature toward the bifurcate channels at the bifurcation. Such upstream influence is also observed in curved channels and may be the result of the actual flow curvature itself [*Jamieson et al.*, 2010], or the result of backwater effects [*Blanckaert et al.*, 2013]. Downstream of the bifurcation, the flow structure shows a pattern that is consistent with plunging water resulting from super-elevation at the bifurcation point, as shown by *Thomas et al.* [2011].

In classical analyses of the stability of a perfectly symmetrical bifurcation, a perturbation to the bed level or water depth is introduced either in one of the distributaries or just upstream of the bifurcation [*Wang et al.*, 1995; *Bolla Pittaluga et al.*, 2003; *Kleinhans et al.*, 2008]. Such a perturbation may grow or dampen depending on the channel width-to-depth ratio and sediment mobility. A growing perturbation may eventually lead to the closure of one of the bifurcate channels, i.e., the bifurcation is unstable. In the present paper, we document laboratory flume experiments in which we perturbed the bifurcation by changing the energy gradient in the bifurcate channels. Theoretically, this should always lead to the enlargement of the channel receiving the most discharge when the bifurcation is otherwise symmetrical. Our experimental findings suggest that the destabilization of a morphologically perfectly symmetrical bifurcation has a pronounced influence on the near-bed flow over a distance of about one channel width upstream of the bifurcation, which may influence the bifurcation stability. This length scale is in agreement with the length scales and model concepts of *Bolla Pittaluga et al.* [2003] and *Kleinhans et al.* [2008]. However, in these models, the upstream length of bifurcation influence is assumed to be the result of an upstream extension of topographic forcing by the bed [e.g., *McArdell and Faeh*, 2001; *Bolla Pittaluga et al.*, 2003; *Kleinhans et al.*, 2008], which was absent in our experiments. In our case, the dividing line between near-bed flow that enters the dominant channel and near-bed flow that enters the subordinate channel is strongly curved (Figure 7). Thus, the fraction of upstream channel width that contributes water to the dominant bifurcate channel is much larger than expected on the basis of the relative discharges of the bifurcate channels. This novel result is not included within the depth-averaged model concepts used in both *Bolla Pittaluga et al.* [2003] and *Kleinhans et al.* [2008]. The implication is that linear stability analyses of perturbed bifurcations based on depth-averaging require modification for the flow structure induced by discharge asymmetry, which is the result of a perturbation in one of the downstream channels.

The observed near-bed flow structure upstream of perturbed bifurcations has an unexpected ramification for the breakdown of symmetry of river bifurcations. In our experiments, near-bed flow is directed toward the dominant bifurcate. Such flow structure may cause an increase of sediment supply into this dominant channel. For example, for experiments where the dominant bifurcate received about 60% of the total discharge, about 70% of the near-bed flow was going into this bifurcate (Figure 7). We expect a similar effect on bed load partitioning in bifurcations.

Morphologically, we suggest that the impact of this accentuated asymmetry on near-bed flow partitioning could be a negative feedback on the destabilized bifurcation: the dominant bifurcate channel could receive so much more sediment that it aggrades, reducing its conveyance and thus forcing the bifurcation toward symmetry. In other words, the net effect opposes the initial degradation of the dominant bifurcate channel, particularly in the case of narrow and deep rivers with stronger transverse flow. Curvature in the flow just

upstream of the bifurcation will initially lead to sedimentation in the dominant channel because of flow convergence, but also sedimentation upstream of the subordinate channel distributary because of flow divergence. As a result, the dominant channel may aggrade initially, even if it eventually enlarges [e.g., *Bertoldi and Tubino*, 2007; *Bolla Pittaluga et al.*, 2003; *Edmonds and Slingerland*, 2008; *Federici and Paola*, 2003; *Kleinhans et al.*, 2008; *Miori et al.*, 2006]. The flow structure observed in our experiments may thus cause stabilization of a symmetrical but perturbed bifurcation. This negative feedback has not been described before.

The question is: how important is this negative feedback in natural bifurcations? It could be argued that the sediment transport capacity of the dominant bifurcate channel would increase nonlinearly with discharge. However, the analyses of *Wang et al.* [1995] and *Bolla Pittaluga et al.* [2003] demonstrate that the ratio of sediment transport in the two bifurcates $Q_{s,right}/Q_{s,left} = (Q_{right}/Q_{left})^k$, where k is unity in the absence of a transverse bed slope and planimetric perturbation. In principle, k is to be determined empirically, but three-dimensional flow and sediment transport modeling has demonstrated that k is approximately unity for much of the lifetimes of bifurcations formed in mobile beds [*Kleinhans et al.*, 2008]. Here $k = 1$ means that sediment is partitioned over the downstream channels proportionally to their widths. This work was based on modeling idealized but asymmetrical bifurcations with an initially flat bed [*Kleinhans et al.*, 2008]. There were indeed fluctuations in discharge partitioning after the start of all model runs, particularly in runs where the bifurcate channels were nearly balanced by, on the one hand, a gradient advantage for one channel, but on the other hand an advantage for the other channel caused by an upstream bend with helical flow upstream of the bifurcation that favored the subordinate channel. The models show that initially sediment always deposited in one of the channels such that k is offset as the dominant bifurcate channel initially receives relatively more sediment despite the presence of a bend [*Kleinhans et al.*, 2008, Figure 9]. This can be expressed empirically as:

$$Q_{s,right}/Q_{s,left} = a(Q_{right}/Q_{left})^k \qquad (14)$$

where $a < 1$. In the numerical model, the ultimate bifurcation condition was asymmetrical in the manner expected from gradient or upstream bend advantage, but the evolution toward this state was delayed by the negative feedback of flow structure.

In short, previous numerical modeling work supports our hypothesis that bifurcations with subcritical flow, perturbed by asymmetrical downstream discharge conveyance, have a flow structure that may result in elevated sediment transport into the dominant channel, providing a negative feedback on the onset of bifurcation destabilization. Given that the transverse bed slope upstream of the bifurcation only overcomes the initial flow and sediment attraction of the advantaged channel in a later stage, we hypothesize that balancing potentially occurs when the transverse bed slope development is limited whilst the imbalance between channel width and flow discharge is large. In other words, balancing flow attraction and sediment attraction is most likely to occur where there is a large gradient or bend advantage for one channel, leading to higher discharge, whilst the other channel is equally wide or wider but has a lower discharge. Other important factors are the roughness of the channel and the width-to-depth ratio of the channel, as these suppress the transverse flow and therefore the sediment attraction of the dominant channel.

The hitherto unidentified effect could lead to unexpected sedimentation in engineered bifurcations, for example, in small streams with newly created side channels. Such altered sedimentation patterns are likely in cases of low roughness. Furthermore, the flow structure and the inherited mixing of flow propagating into the downstream branches may be relevant for the aquatic chemistry of small bifurcating streams as commonly found in lowland areas, because it modifies the supply of dissolved oxygen, nutrients and organic matter. In addition, the reported effects of bifurcation perturbation on near-bed flow affect the biologically important benthic boundary layer.

5. Conclusions

The effect of flow structure on the stability of geometrically symmetrical bifurcations was studied in fixed-bed experiments under a range of conditions, including both a smooth and rough bed case, over two

width-to-depth ratios and either symmetrical or asymmetrical flow division forced by downstream water surface gradient.

Upstream of the bifurcation, counter-rotating flow structures emerged. In high width-to-depth ratio channels, the number of flow cells increased. These flow cells were equal in size for bifurcations with equal discharge division, but asymmetrical for the bifurcation with unequal discharge division. The flow cells diminished in strength with higher width-to-depth ratio and bed roughness. Closer to the bifurcation, flow divergence suppressed the flow structures.

Our experiments demonstrate that, under unequal discharge division, the flow is strongly curved toward the channel with the highest discharge over a length of about one channel width. The near-bed flow curvature was considerably larger than the surface flow curvature, with the strongest curvature just upstream of the bifurcation. These effects diminish with increasing width-to-depth ratio and increasing bed roughness.

Our results imply that a disproportionately large amount of sediment can be transported into the downstream channel with the largest discharge. This could provide a negative feedback on bifurcation destabilization because the enhanced sediment input would reduce the expected erosion rate in that channel. This modifies the usual hypothesis that sediment division in a symmetrical bifurcation is proportional to channel width. This mechanism would act as a stabilizing effect on perturbed river bifurcations, which has not been taken into account in current theory.

References

Adrian, R. J. (1991), Particle-imaging techniques for experimental fluid mechanics, *Annu. Rev. Fluid Mech.*, *23*(1), 261–304, doi:10.1146/annurev.fl.23.010191.001401.

Adrian, R. J. (2005), Twenty years of particle image velocimetry, *Exp. Fluids*, *39*(2), 159–169, doi:10.1007/s00348-005-0991-7.

Bertoldi, W., and M. Tubino (2005), Bed and bank evolution of bifurcating channels, *Water Resour. Res.*, *41*, W07001, doi:10.1029/2004WR003333.

Bertoldi, W., and M. Tubino (2007), River bifurcations: Experimental observations on equilibrium configurations, *Water Resour. Res.*, *43*, W10437, doi:10.1029/2007WR005907.

Blanckaert, K., M. G. Kleinhans, S. J. McLelland, W. S. J. Uijttewaal, B. J. Murphy, A. van de Kruijs, D. R. Parsons, and Q. Chen (2013), Flow separation at the inner (convex) and outer (concave) banks of constant-width and widening open-channel bends, *Earth Surf. Processes Landforms*, *38*(7), 696–716, doi:10.1002/esp.3324.

Bolla Pittaluga, M., R. Repetto, and M. Tubino (2003), Channel bifurcation in braided rivers: Equilibrium configurations and stability, *Water Resour. Res.*, *39*(3), 1046, doi:10.1029/2001WR001112.

Bradbrook, K. F., S. N. Lane, K. S. Richards, P. M. Biron, and A. G. Roy (2001), Role of bed discordance at asymmetrical river confluences, *J. Hydraul. Eng.*, *127*(5), 351–368, doi:10.1061/(ASCE)0733-9429(2001)127:5(351).

Buffin-Bélanger, T., and A. G. Roy (2005), 1 min in the life of a river: Selecting the optimal record length for the measurement of turbulence in fluvial boundary layers, *Geomorphology*, *68*(1–2), 77–94, doi:10.1016/j.geomorph.2004.09.032.

Edmonds, D. A., and R. L. Slingerland (2008), Stability of delta distributary networks and their bifurcations, *Water Resour. Res.*, *44*, W09426, doi:10.1029/2008WR006992.

Edmonds, D. A., and R. L. Slingerland (2009), Significant effect of sediment cohesion on delta morphology, *Nat. Geosci.*, *3*(2), 105–109, doi:10.1038/ngeo730.

Federici, B., and C. Paola (2003), Dynamics of channel bifurcations in noncohesive sediments, *Water Resour. Res.*, *39*(6), 1162, doi:10.1029/2002WR001434.

Gui, L., and W. Merzkirch (1996), A method of tracking ensembles of particle images, *Exp. Fluids*, *21*(6), 465–468, doi:10.1007/BF00189049.

Jamieson, E., G. Post, and C. Rennie (2010), Spatial variability of three-dimensional Reynolds stresses in a developing channel bend, *Earth Surf. Processes Landforms*, *35*(9), 1029–1043, doi:10.1002/esp.1930.

Jodeau, M., A. Hauet, A. Paquier, J. Le Coz, and G. Dramais (2008), Application and evaluation of LS-PIV technique for the monitoring of river surface velocities in high flow conditions, *Flow Meas. Instrum.*, *19*(2), 117–127, doi:10.1016/j.flowmeasinst.2007.11.004.

Klaassen, G. J., and G. Masselink (1992), Planform changes of a braided river with fine sand as bed and bank material, in: Larsen, P. and N.E. Eisenhauer (Eds.), Sediment Management: *Proceeding of 5th International Symposium on River Sedimentation*, pp. 459–471, Karlsruhe, Germany.

Kleinhans, M. G., H. R. A. Jagers, E. Mosselman, and C. J. Sloff (2008), Bifurcation dynamics and avulsion duration in meandering rivers by one-dimensional and three-dimensional models, *Water Resour. Res.*, *44*, W08454, doi:10.1029/2007WR005912.

Kleinhans, M. G., K. M. Cohen, J. Hoekstra, and J. M. IJmker (2011), Evolution of a bifurcation in a meandering river with adjustable channel widths, Rhine delta apex, The Netherlands, *Earth Surf. Processes Landforms*, *36*(15), 2011–2027, doi:10.1002/esp.2222.

Kleinhans, M. G., T. Haas, E. Lavooi, and B. Makaske (2012), Evaluating competing hypotheses for the origin and dynamics of river anastomosis, *Earth Surf. Processes Landforms*, *37*(12), 1337–1351, doi:10.1002/esp.3282.

Kleinhans, M. G., R. I. Ferguson, S. N. Lane, and R. J. Hardy (2013), Splitting rivers at their seams: Bifurcations and avulsion, *Earth Surf. Processes Landforms*, *38*(1), 47–61, doi:10.1002/esp.3268.

McArdell, B., and R. Faeh (2001), A computational investigation of river braiding, in *Gravel-Bed Rivers V*, edited by M. Mosley, pp. 73–94, N. Z. Hydrol. Soc., Wellington.

Merzkirch, W., and L. Gui (2000), A comparative study of the MQD method and several correlation-based PIV evaluation algorithms, *Exp. Fluids*, *28*(1), 36–44, doi:10.1007/s003480050005.

Miori, S., R. Repetto, and M. Tubino (2006), A one-dimensional model of bifurcations in gravel bed channels with erodible banks, *Water Resour. Res.*, *42*, W11413, doi:10.1029/2006WR004863.

Mori, N., and K.-A. Chang (2003), Introduction to MPIV, user reference manual, p. 14. [Available at: http://www.oceanwave.jp/softwares/mpiv.]

Parker, G. (2004), E-book: 1D sediment transport morphodynamics with applications to rivers and turbidity currents. [Available at: http://vtchl.uiuc.edu/people/parkerg/morphodynamics_e-book.htm.]

Parsons, D. R., J. L. Best, S. N. Lane, O. Orfeo, R. J. Hardy, and R. Kostaschuk (2007), Form roughness and the absence of secondary flow in a large confluence-diffluence, Rio Paraná, Argentina, *Earth Surf. Processes Landforms*, *32*(1), 155–162, doi:10.1002/esp.1457.

Peakall, J., and J. Warburton (1996), Surface tension in small hydraulic river models—The significance of the Weber number, *J. Hydrol. N. Z.*, *35*(2), 199–212.

Ramamurthy, A. S., J. Qu, and D. Vo (2007), Numerical and experimental study of dividing open-channel flows, *J. Hydraul. Eng.*, *133*(10), 1135–1144, doi:10.1061/(ASCE)0733-9429(2007)133:10(1135).

Repetto, R., M. Tubino, and C. Paola (2002), Planimetric instability of channels with variable width, *J. Fluid Mech.*, *457*, 79–109, doi:10.1017/S0022112001007595.

Ribberink, J. S., and J. T. M. Van Der Sande (1985), Aggradation in rivers due to overloading—Analytical approaches, *J. Hydraul. Res.*, *23*(3), 273–283, doi:10.1080/00221688509499355.

Shettar, A. S., and K. Keshava Murthy (1996), A numerical study of division of flow in open channels, *J. Hydraul. Res.*, *34*(5), 651–675, doi: 10.1080/00221689609498464.

Slingerland, R. L., and N. D. Smith (2004), River avulsions and their deposits, *Annu. Rev. Earth Planet. Sci.*, *32*(1), 257–285, doi:10.1146/annurev.earth.32.101802.120201.

Takeda, Y. (1991), Development of an ultrasound velocity profile monitor, *Nucl. Eng. Des.*, *126*(2), 277–284, doi:10.1016/0029–5493(91)90117-Z.

Takeda, Y. (1995), Velocity profile measurement by ultrasonic Doppler method, *Exp. Therm. Fluid Sci.*, *10*(4), 444–453, doi:10.1016/0894–1777(94)00124-Q.

Thomas, R. E., D. R. Parsons, S. D. Sandbach, G. M. Keevil, W. A. Marra, R. J. Hardy, J. L. Best, S. N. Lane, and J. A. Ross (2011), An experimental study of discharge partitioning and flow structure at symmetrical bifurcations, *Earth Surf. Processes Landforms*, *36*(15), 2069–2082, doi: 10.1002/esp.2231.

van Balen, W. (2010), Curved open-channel flows, PhD thesis, TU Delft, Delft.

Wang, Z., M. De Vries, R. Fokkink, and A. Langerak (1995), Stability of river bifurcations in 1D morphodynamic models, *J. Hydraul. Res.*, *33*(6), 739–750, doi:10.1080/00221689509498549.